Scientific Contributions Oil & Gas, Vol. 49. No. 2, June: 173 - 201

SCIENTIFIC CONTRIBUTIONS OIL AND GAS

Testing Center for Oil and Gas
LEMIGAS

Journal Homepage:http://journal.lemigas.esdm.go.id
ISSN: 2089-3361, e-ISSN: 2541-0520

Optimizing CO_2 Storage Strategies for Enhanced Mineral Trapping and Plume Containment in The Aquifer Zone of an Indonesian Gas Reservoir

Utomo Pratama Iskandar, Arik, Panuju, Garindia Grandis, and Nanda Ilham

Oil and Gas Testing Center LEMIGAS
Ciledug Raya Street, No. 109, Cipulir, Kebayoran Lama Subdistrict, South Jakarta, 12230, Indonesia.

Corresponding author: Utomo Pratama Iskandar (utomo.iskandar@esdm.go.id)

Manuscript received: February 10th, 2026; Revised: March 17th, 2026
Approved: April 28th, 2026; Available online: June 08th, 2026; Published: June 08th, 2026.

ABSTRACT - This study evaluates optimized CO_2 storage strategies in the aquifer zone of the SK gas field in Indonesia to improve plume containment and explore the potential for enhanced mineral trapping. A coupled compositional-flow and reactive-transport simulation workflow was applied using an upscaled reservoir model under a common safe operating pressure envelope and a containment constraint requiring the plume to remain within the aquifer zone over a 120-year simulation period. Three groups of scenarios were examined: well-placement sensitivity (A1–A3), production-assisted injection (B1–B3), and completion-design sensitivity (C1–C3). Among the baseline cases, A3 provided the best plume containment, with the most compact lateral footprint and smallest vertical plume spread, while A1 gave the highest total stored CO_2. Among the production-assisted cases, B2 was the most effective pressure-management option, producing the largest pressure reduction and a modest increase in total stored CO_2. Completion redesign generated the largest storage gains, increasing total stored CO_2 by about 28–33.3% relative to the corresponding baseline cases. Most scenarios maintained the plume confinement within the aquifer zone, although C1 showed localized upward CO_2 occurrence near the free-water level. Overall, the tested strategies improved storage performance, with A3 providing the best plume containment among the baseline cases, B2 delivering the strongest pressure-management benefit and increasing total stored CO_2 by approximately 3.93% relative to A2, and completion redesign producing the largest storage gains, increasing total stored CO_2 by about 28–33.3% relative to the corresponding baseline cases. Mineral trapping increased slightly in the completion-design cases, although it remained a minor component of total storage within the 120-year simulation period.

Keywords: carbon capture and storage (CCS), aquifer-zone CO_2 injection, gas reservoir aquifer, plume containment

How to cite this article:

Utomo Pratama Iskandar, Arik, Panuju, Garindia Grandis, and Nanda Ilham, 2026, Optimizing CO_2 Storage Strategies for Enhanced Mineral Trapping and Plume Containment in The Aquifer Zone of an Indonesian Gas Reservoir, Scientific Contributions Oil and Gas, 49 (2) pp. 173-201. DOI org/10.29017/scog.v49i2.2067.

INTRODUCTION

Carbon capture and storage (CCS) is increasingly positioned as a time-critical mitigation option because many climate-stabilization pathways require the rapid scale-up of CO_2 capture and durable geological storage. In addition, practical deployment constraints mean that delaying large-scale CCS would make it substantially harder to achieve stringent temperature targets (Kazlou et al., 2024; Iskandar 2009). In Indonesia, this urgency is reinforced by the national commitment to achieve net-zero emissions by 2060. However, analyses of the country's energy-policy landscape indicate that institutional, financing, and coordination barriers must still be addressed alongside sector-specific technical constraints (Massagony et al., 2025). These conditions make the identification of technically robust and storage-secure geological settings an important research priority.

Among the available geological storage options, depleted hydrocarbon reservoirs and their associated aquifers have received increasing attention as technically viable and economically attractive targets. In particular, aquifer-zone injection in gas reservoirs offers strategic advantages because such systems commonly benefit from demonstrated trapping integrity, extensive subsurface characterization, and reusable infrastructure, thereby reducing development cost and uncertainty (van den Hoek et al., 2025). A water leg aquifer is defined as the brine-saturated portion of a reservoir located beneath or laterally adjacent to an oil or gas accumulation, where the pore space is occupied mainly by saline formation water (Worden 2024). In gas reservoirs, this water leg is hydraulically connected to the gas-bearing interval through the gas–water contact, and its flow behavior is governed by the same structural and stratigraphic architecture that originally trapped buoyant hydrocarbons. Compared with virgin deep saline aquifers, such systems may offer better-constrained pressure histories, existing infrastructure, and greater operational understanding of reservoir connectivity and pressure management (Hoteit et al., 2019; Akai et al., 2021; Khanifar et al., 2024; Zaidin et al., 2018). Global assessments have similarly highlighted depleted gas reservoirs as among the most mature and technically understood geological storage systems (IPCC 2022; Global CCS Institute 2023).

Despite these advantages, CO_2 storage in the aquifer leg of a gas reservoir presents a distinct operational challenge. Because CO_2 is buoyant, plume migration may proceed upward and updip, increasing the risk of encroachment toward the hydrocarbon zone, particularly where reservoir heterogeneity and permeability anisotropy promote preferential flow pathways. At the same time, aquifer pressure behavior and boundary conditions strongly influence the magnitude and spatial extent of pressure buildup during injection, which in turn affects injectivity, geomechanical stability, and long-term containment security (Worden 2024; Martin-Roberts et al., 2021; White et al., 2014). Previous project experience, especially at In Salah, has demonstrated the practical feasibility of injection into aquifer systems associated with gas reservoirs, while also underscoring the importance of managing reservoir pressure and preserving containment integrity (Mathieson et al., 2011; Ringrose et al., 2013; Rucci et al., 2013; Vasco et al., 2010). In parallel, mineral trapping is widely regarded as a favorable long-term storage mechanism, yet it generally develops slowly under reservoir conditions. Although prior studies widely report trapping contributions in saline aquifers and depleted reservoir settings (Al-Hajri & Al-Maldas 2026; Chai et al., 2025; Medeiros et al., 2025; Wang et al., 2025; Zhang et al., 2024), fewer studies explicitly treat aquifer-only plume containment as an operational design constraint (Iskandar & Kurihara 2022), and relatively few evaluate the combined influence of injection control, well placement, completion design, and production-assisted pressure management within a single integrated framework for gas-reservoir aquifer legs.

These challenges are particularly relevant for Indonesian gas reservoirs. The SK Gas Field, located onshore in the South Sumatra Basin, provides a representative setting for evaluating aquifer-zone CO_2 storage in a geologically realistic Indonesian context. The field is associated with established gas production and transmission infrastructure. It is situated in a basin where hydrocarbon accumulations commonly occur in basement-influenced structural highs and Miocene carbonate buildups. The reservoir interval of interest is associated with the Baturaja Formation. It is vertically bounded by sealing shale units, creating a stacked carbonate–marine shale architecture that is favorable for long-term containment. In addition, facies variability and diagenetic overprint within the carbonate reservoir generate heterogeneity, permeability anisotropy, and internal baffles, likely influencing plume migration behavior and trapping efficiency. Despite these favorable characteristics, optimization-focused CCS studies for Indonesian gas reservoirs such as the SK Gas Field remain limited (Iskandar & Kurihara 2025).

This study aims to develop and evaluate an optimized CO_2 storage strategy for the aquifer zone of the SK Gas Field that ensures pressure-safe and containment-secure geological storage while enhancing long-term mineral trapping. The analysis integrates injection-parameter optimization, including injection scheme and well configuration, under caprock, fault, fracture, and regulatory constraints, with dynamic assessment of plume migration and pressure evolution. Time-lapse plume evolution and pressure-distribution maps are used to identify zones of maximum pressure buildup and dominant flow pathways, providing insight into potential leakage risks. The study further quantifies the temporal progression of mineral trapping, evaluates the relative contributions of different trapping mechanisms to permanent CO_2 storage, ensures that the plume remains within the licensed boundary, and assesses the influence of production operations on storage performance.

METHODOLOGY

This study adopted a constraint-based simulation workflow to evaluate and compare alternative CO_2 storage strategies in the SK gas reservoir's aquifer zone. The methodology was designed to quantify the effects of well placement, production-assisted injection, and completion design on plume containment, pressure response, injectivity, and trapping evolution under a common set of operational and containment constraints. The overall workflow consisted of six main stages: static-model upscaling, local grid refinement, construction of the fluid and geochemical models, scenario implementation, constraint enforcement, and performance evaluation.

Overall workflow

The study workflow is summarized in Figure 1. This workflow was developed to ensure that all tested cases were evaluated consistently, using the same reservoir model, fluid description, geochemical assumptions, simulation period, and storage-security criteria. In this way, differences in model outcomes could be attributed primarily to the investigated design variables rather than to changes in model formulation.

Static-model upscaling

The original fine-scale geological model was upscaled prior to dynamic simulation to reduce computational cost while preserving the key heterogeneity controls governing CO_2 migration and pressure propagation. The initial static model consisted of 6,683,915 cells distributed over 528 vertical layers. This model was coarsened to 478,336 cells and 37 layers for compositional and reactive transport simulations. Property upscaling was performed using variable-specific averaging methods consistent with their physical behavior. Porosity was upscaled by arithmetic averaging, permeability by directional arithmetic-harmonic averaging, and water saturation by geometric averaging. The lateral cell size was maintained at 100 m x 100 m to preserve areal reservoir architecture, whereas the vertical grid spacing was increased to 50 ft in Zones A-C and 40 ft in Zones D-E. This approach reduced numerical burden while retaining the stratigraphic layering and the main heterogeneity patterns relevant to plume migration, injectivity, and trapping behavior.

Local grid refinement

To improve the representation of near-well flow processes, local grid refinement (LGR) was applied around each injection well. This step was necessary because the coarsened simulation grid alone was insufficient to capture steep pressure gradients, early saturation changes, and the near-well dissolution-reaction zone that controls injectivity and early-time plume development. Cartesian LGR was implemented in the Nx, Ny, and Nz directions, with a refinement factor of 2. As a result, the refined cells near the well had a horizontal dimension of 50 m x 50 m, and the number of vertical layers was doubled locally. The refinement zone extended to approximately 300 m from the wellbore. This approach provided a more accurate representation of near-well pressure buildup, CO_2 saturation fronts, and local reactive processes without imposing the computational burden of a fully fine-scale grid over the entire model domain.

Fluid-property characterization and compositional model

Multiphase flow and phase behavior were simulated using the CMG-GEM compositional simulator. A simplified binary fluid description was adopted, consisting of injected CO_2 and a lumped native-gas component representing the dominant reservoir gas. This formulation was selected to provide a computationally efficient yet physically consistent representation of fluid-phase behavior during injection and post-injection migration. Formation-water properties were defined as functions of pressure, temperature, and salinity. Brine density was calculated using the Rowe and Chou correlation, and brine viscosity was estimated using the Kestin correlation. Mutual solubility between CO_2 and brine was represented using Harvey's method, assuming local thermodynamic equilibrium between the gaseous and aqueous phases. These formulations enabled the model to represent CO_2 dissolution into formation water and its contribution to solubility trapping during the simulation period.

Reactive-transport and geochemical model

Reactive transport was incorporated to evaluate the evolution of geochemical trapping, particularly mineral trapping, during long-term CO_2 storage. The mineral system was simplified to the dominant carbonate minerals in the reservoir: calcite and dolomite. This simplification was adopted to focus the simulation on the principal carbonate reactions governing dissolution and precipitation in the studied reservoir system.

Aqueous reactions and CO_2 speciation in brine were assumed to reach local equilibrium, while mineral reactions were treated as kinetic processes. Dissolved CO_2 was allowed to form carbonic acid, which then dissociated into bicarbonate and carbonate species, altering brine chemistry and driving carbonate dissolution and precipitation reactions. For calcite, the reactive surface area was set to 88 m^2/m^3, the logarithmic rate constant to -8.79588, and the activation energy to 41,870 J/mol. For dolomite, the reactive surface area was also set to 88 m^2/m^3, with a logarithmic rate constant of -9.2218 and an activation energy of 41,870 J/mol. These parameters were used consistently across all scenarios to ensure that differences in mineral trapping resulted from flow behavior and operational design rather than from changes in geochemical parameters.

Scenario design

A systematic scenario-based design was used to assess the influence of operational and well-design variables on storage performance (Table 1). All scenarios were simulated using the same reservoir grid, fluid-property formulation, geochemical model, simulation period, and operational constraint framework. Therefore, each scenario isolated the effect of a specific design variable.

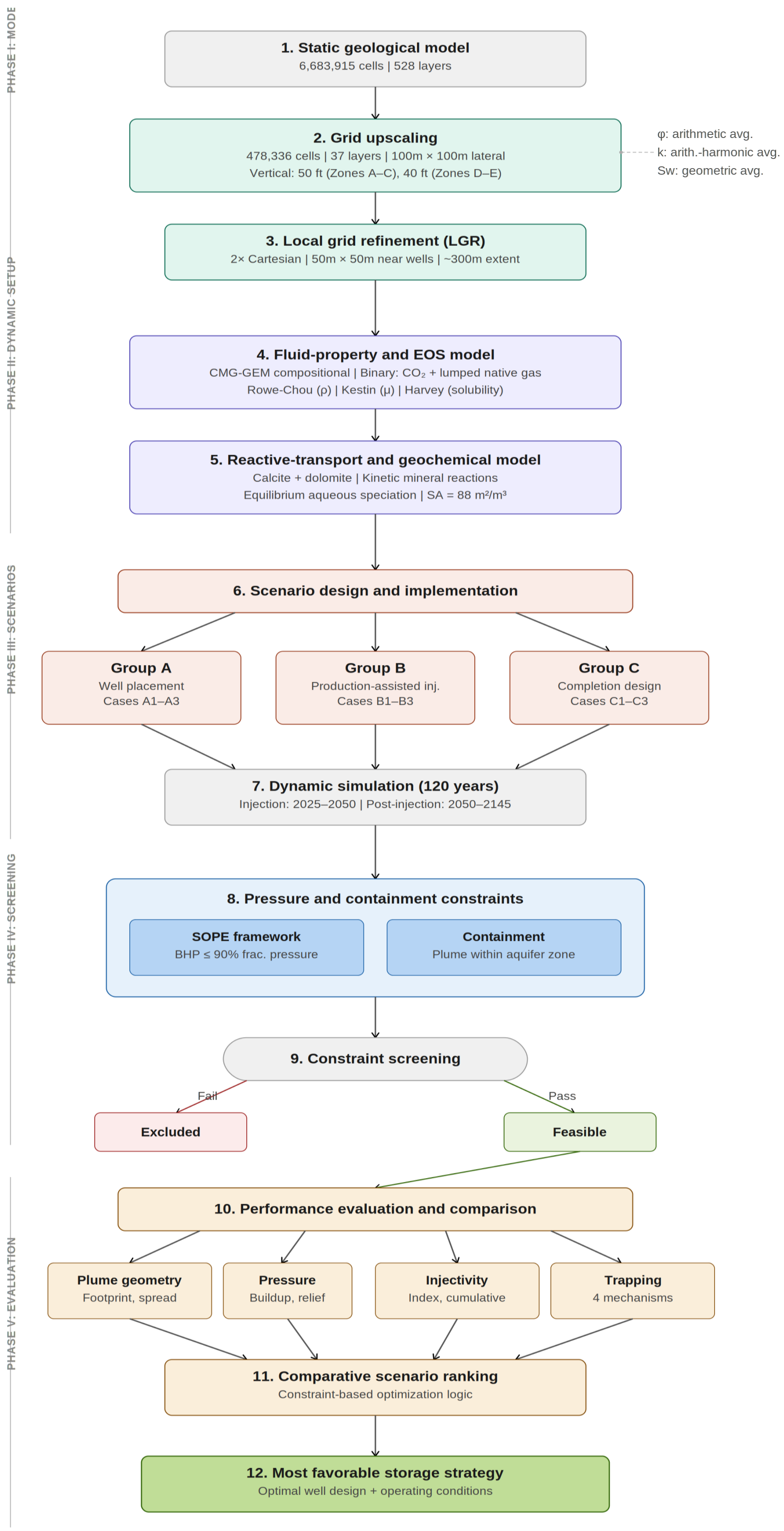

Figure 1. Workflow of the constraint-based simulation methodology for CO_2 storage optimization in the SK aquifer zone

Simulation period and operating conditions

All simulations covered a total period of 120 years. CO2 injection was modeled from 2025 to 2050, corresponding to a 25-year operational period, followed by a 95-year post-injection period ending in 2145. This time window was selected to capture both active injection behavior and the longer-term redistribution of pressure and trapping mechanisms after injection ceased. All scenarios were evaluated under the same general operating philosophy. Injection was allowed to proceed until the pressure-constraint framework imposed a limit. This enabled direct comparison of pressure-limited storage performance, plume migration, and trapping evolution across all cases.

Pressure and containment constraints

All scenarios were evaluated within a common storage-security framework comprising pressure and containment constraints. Pressure limitation was implemented through a Safe Operating Pressure Envelope (SOPE), in which the maximum allowable injection pressure was set to the minimum of the relevant failure thresholds: fracture pressure, fault-slip pressure, tensile failure pressure, and caprock entry pressure.

Operationally, the model applied a bottom-hole pressure limit corresponding to approximately 90% of the fracture pressure. This was used as a practical safeguard to reduce the likelihood of fracture initiation and to preserve the mechanical integrity of the reservoir-caprock system during CO_2 injection. Containment was imposed as a hard performance condition. The CO_2 plume was required to remain within the aquifer zone throughout the simulation period, with no intentional upward migration into the hydrocarbon interval. This criterion was essential because the study objective was not only to increase the amount of CO_2 stored but also to maintain plume confinement within the designated storage interval.

Performance metrics and comparative evaluation

Scenario performance was evaluated using a consistent set of dynamic and geochemical metrics. These included plume geometry, pressure behavior, injectivity, total stored CO_2, and trapping contribution. Plume geometry was assessed based on lateral footprint, migration distance, and vertical spread. Pressure response was examined using pressure-distribution maps, which showed localized pressure reduction near the injector and at the reservoir top. Injectivity performance was assessed through the injectivity index behavior and the cumulative storage response under the applied constraints. Storage security and permanence were evaluated by simulating the contributions of the main trapping mechanisms: supercritical or structural trapping, residual trapping, solubility trapping, and mineral trapping. These metrics were compared among all cases to identify which strategies improved storage performance while preserving containment and pressure safety.

Methodological basis for optimization

Although the study was implemented through systematic scenario screening rather than formal mathematical optimization, the methodological logic was optimization-oriented. A reference case was first established, after which alternative operational designs were tested one variable at a time. Each scenario was then assessed against the same pressure and containment constraints and compared using common performance metrics. In this sense, the workflow served as a constraint-based optimization approach, identifying the most favorable storage strategy by ranking feasible scenarios based on pressure behavior, plume containment, injectivity, and long-term trapping performance.

RESULT AND DISCUSSION

Reservoir description

The SK Field is characterized by a saline aquifer system within the Baturaja Formation, where the formation brine has an initial salinity of approximately 15,000 ppm NaCl, a measured water resistivity of 0.25 ohm-m at 75 °F, and an aqueous density of about 1,020 kg/m³, indicating moderately saline formation water. Reservoir temperatures range from 266.6 to 315.2 °F (≈130.3 –157.3 °C), while initial reservoir pressure is reported between 3,943.96 and 3,994.9 psia,

Table 1. Summary of CO_2 injection scenarios and investigated variables

Scenario group	Cases	Main variable tested	Configuration summary	Main purpose	Key outcomes evaluated
Well placement	A1–A3	Injector location	Single injector placed at different structural positions within the aquifer zone	To identify the injector location that gives the best balance between storage performance, plume containment, and pressure behavior	Plume geometry, migration pathway, pressure buildup, trapping evolution
Production-assisted injection	B1–B3	Addition and position of the producer well	Same injector as baseline, with one producer added in the gas zone at varying distances and locations	To assess whether gas production can reduce pressure, improve injectivity, steer plume migration, and enhance storage performance	Pressure relief, injectivity, plume steering, storage performance, upward migration risk
Completion design	C1–C3	Completion interval and perforation extent	Same injector location and operating constraints, but different completion designs	To determine whether increased well–reservoir contact can improve injectivity and storage while maintaining plume containment	Near-well pressure distribution, vertical and lateral plume growth, injectivity, trapping mechanism evolution

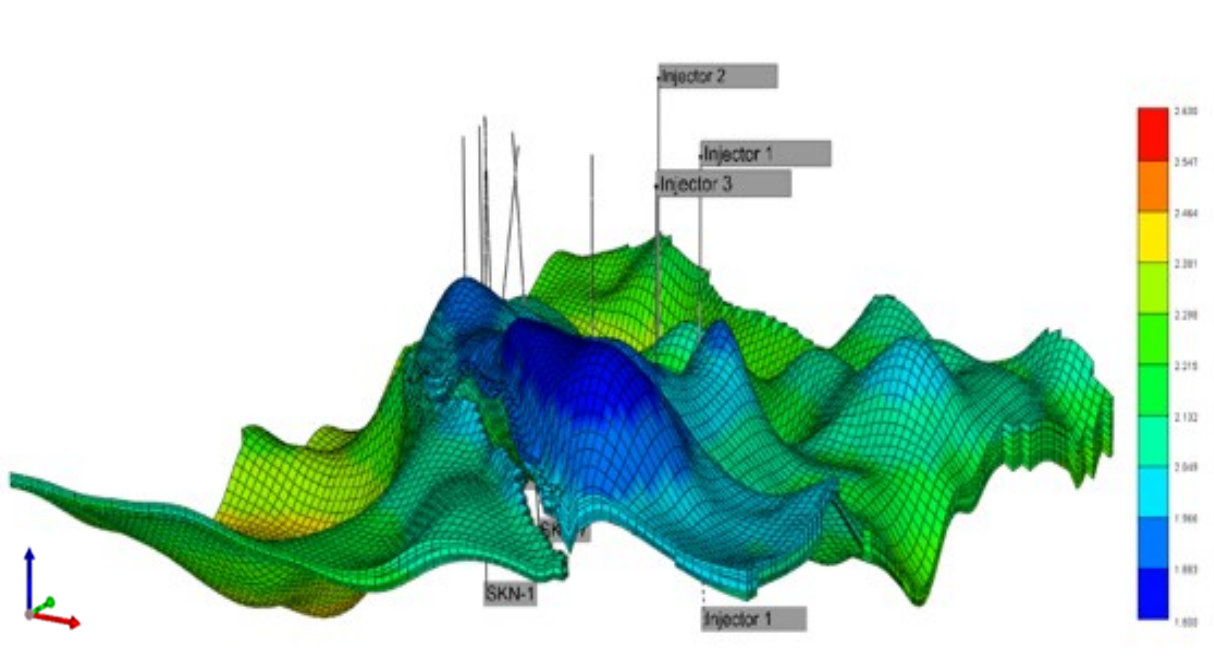

Figure 2. The SK reservoir model field

corresponding to an initial pressure of 27,545.3 kPa at a datum depth of 2,169.95 m (Figure 2). Mineralogically, the reservoir is dominated by limestone facies (packstone and wackestone) with skeletal components such as coral and foraminifera, accompanied by micrite envelopes, syntaxial cement, and minor pyrite; for geochemical modeling, calcite and dolomite are identified as the primary reactive minerals governing carbonate precipitation and mineral trapping. The target aquifer for CO_2 injection is primarily Zone 4 (limestone), located between 6,746.5 and 7,511 ft TVD, with additional contributions from Zones D and E, forming a laterally connected aquifer system beneath the gas column. Initial reservoir conditions reflect water-saturated aquifer intervals at in-situ temperature and pressure, providing the baseline state for subsequent CO_2 injection and reactive transport analysis.

Well placement scenario

This scenario serves as the base case, evaluating how alternative injector positions within the reservoir structure influence CO_2 plume migration and containment behavior. It establishes a reference for plume geometry, flow pathways, and heterogeneity effects against which all other scenarios are compared.

Plume geometry

Case A1 shows a plume (Figure 3 a) that is laterally extensive but not maximally aggressive, with a geometry that strongly reflects reservoir-heterogeneity control rather than a smooth, radial expansion. The simulated plume reaches a migration radius of ~829 m and an overall width of ~1,605 m, indicating broad areal spreading in the aquifer, though less expansive than the more extreme lateral-growth behavior observed in A2. In the vertical direction, the plume exhibits a moderate rise of ~196 m, which is consistent with partial vertical restriction (Figure 4 (a)), for example, reduced vertical permeability (low Kv/Kh), intra-reservoir layering, or the absence of a direct vertical high-permeability conduit that would otherwise promote stronger buoyant ascent. The CO_2 distribution does not show an obvious punch-through into the gas zone in the visible maps, suggesting that the plume remains contained below the FWL reference and below the hydrocarbon zone for this well placement.

Case A2 (Figure 3 b) exhibits the least favorable containment geometry among the placement scenarios, with the plume reaching the greatest migration distance (~1,026 m) and the widest footprint (~1,809 m), consistent with stronger lateral connectivity near injector 2. The plume also shows the largest vertical spread (~324 m), indicating significant vertical connectivity that could be enabled by locally higher vertical permeability, cross-layer transmissibility, or a structural/stratigraphic pathway promoting updip rise (Figure 4 (b). This vertical behavior is directly relevant to the FWL and gas-zone objective because the larger rise reduces the buffer to the hydrocarbon zone and places A2 closest to the FWL reference, thereby increasing the containment risk margin relative to A1 and A3. At the same time, the CO_2 distribution does not show clear upward encroachment into the gas zone in the visible maps, suggesting that the plume remains confined below the FWL reference and below the hydrocarbon zone for this well placement. However, the reduced separation implies that the most rigorous near-FWL diagnostics should be applied.

Case A3 (Figure 3 c) exhibits the most favorable geometric containment among the placement scenarios. Although the migration distance reaches ~843 m (comparable to A1), the plume remains markedly more compact because the vertical spread is the smallest (~141 m) and the lateral footprint is the tightest (width ~1,029 m). Taken together, these metrics indicate that buoyancy-driven upward migration is most effectively suppressed in A3, with limited vertical communication developing away from the injector (Figure 4 (c)) and a reduced tendency for updip rise relative to A1 and especially A2. As a result, A3 is interpreted to have the lowest likelihood of gas-zone encroachment among the three cases. Consistent with this interpretation, the CO_2 distribution does not show an obvious upward breakthrough into the gas zone in the visible maps, suggesting that the plume remains confined below the FWL reference and below the hydrocarbon zone for this well placement. At the same time, continued attention is warranted to any localized near-well vertical conduit effects.

Preferential flow pathway

Case A1 exhibits a clear preferential-flow signature expressed as channeling and fingering in the zoomed plume panel (Figure 5), indicating that plume evolution is governed by heterogeneity rather than forming a smooth, symmetric footprint. The lateral permeability distribution (Permeability-i) around the injector exhibits pronounced small-scale spatial variability, creating nonuniform lateral transmissibility and promoting preferential advancement along locally higher-transmissibility directions. In contrast, the vertical permeability distribution (Permeability-k) does not indicate a strongly connected high-permeability feature that would systematically enhance vertical communication across multiple layers. Taken

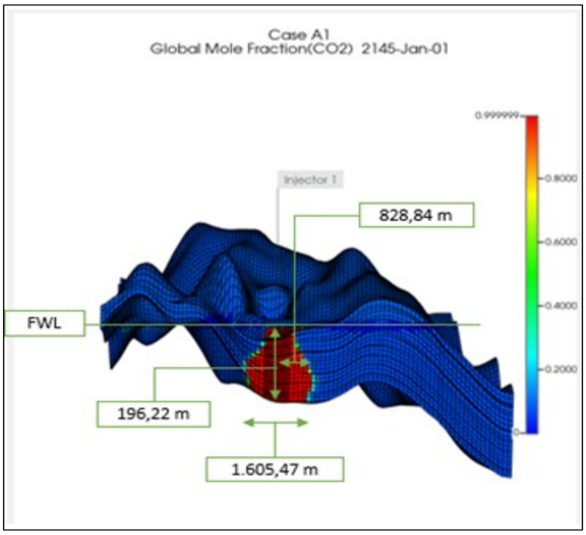

a

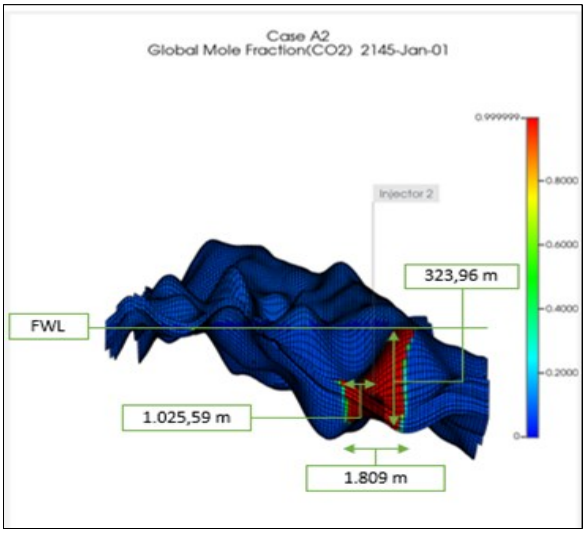

b

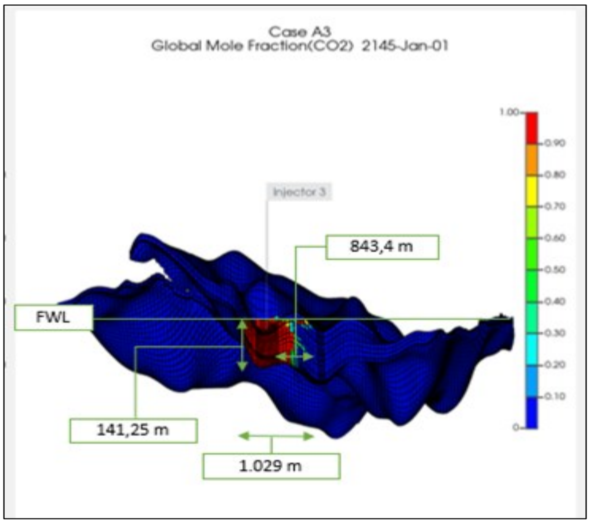

c

Figure 3. CO_2 plume geometry for well placement scenarios at 2145. (a) Case A1, (b) Case A2, and (c) Case A3 showing the spatial distribution of CO_2 mole fraction within the aquifer zone. The horizontal green line represents the free-water level (FWL), indicating the boundary between the aquifer and the overlying gas zone. Annotated values indicate key plume metrics, including lateral migration distance, plume width, and vertical plume rise relative to the injection point.

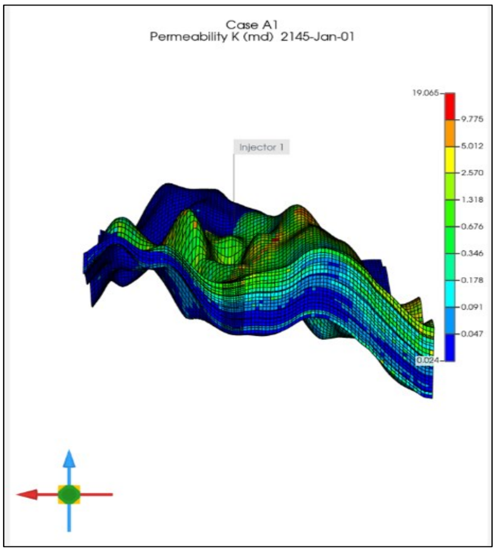

a

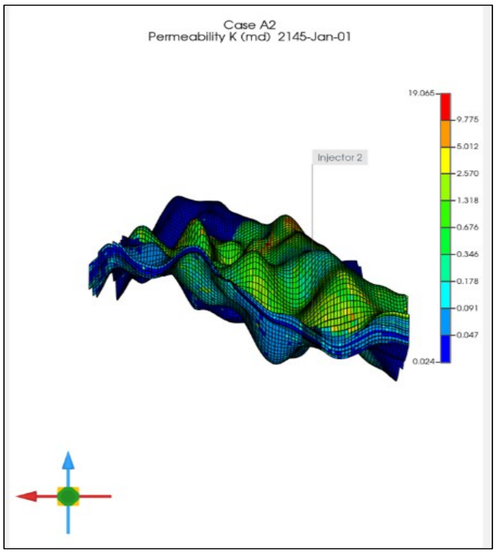

b

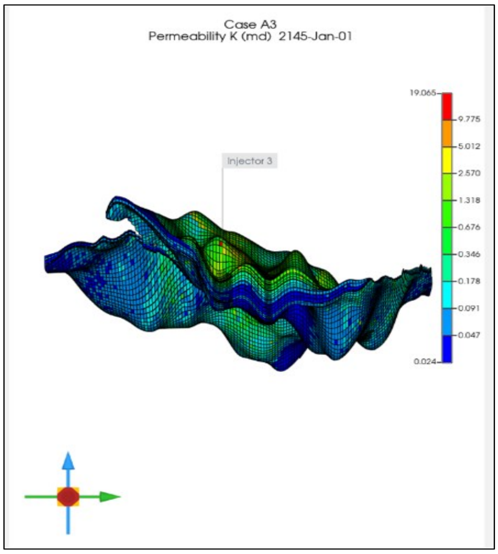

c

Figure 4. Vertical permeability (k_x) distribution for well placement scenarios. (a) Case A1, (b) Case A2, and (c) Case A3 showing spatial variation of vertical permeability (k_v, mD) within the reservoir. The color scale represents permeability magnitude, highlighting heterogeneity and potential vertical connectivity pathways that influence CO_2 plume migration.

together, these maps support the interpretation that A1 is dominated by heterogeneity-controlled lateral migration, where localized preferential pathways can extend lateral movement without necessarily increasing the likelihood of sustained upward propagation, provided that vertical connectivity remains limited.

Case A2 shows the strongest directional preference, with plume development dominated by a single high-mobility pathway rather than distributed fingering, consistent with the presence of a connected lateral high-transmissibility feature. The Permeability-i map suggests a more coherent laterally connected high-permeability trend near the injector relative to A1, which focuses flow and produces an elongated plume aligned with that dominant lateral transmissibility direction. The Permeability-k distribution also suggests that vertical permeability is not uniformly low in the injector vicinity, thereby permitting vertical redistribution where local connectivity exists, particularly over long-time scales when buoyancy contributes to upward migration. This combination typically reduces areal sweep efficiency through bypassing of adjacent pore volume, concentrates mobile CO_2 transport along the preferred direction, and can reduce CO_2–brine contact outside the dominant pathway, thereby increasing sensitivity to heterogeneity and elevating the potential for far-field migration in the preferred direction.

Case A3 displays a preferential-flow signature that is primarily localized near the injector and does not indicate a long-range, laterally connected high-transmissibility feature, which is consistent with its more compact plume behavior. The Permeability-i map indicates a stronger lateral permeability contrast, with relatively higher permeability concentrated near the injector and a more rapid transition to lower permeability farther from the well, limiting long-distance lateral communication and promoting local accumulation. The Permeability-k map suggests a layered vertical permeability structure that supports restricted vertical communication at the model scale; however, the near-well plume strengthening suggests that localized vertical transmissibility near the injector could still influence early redistribution. Accordingly, the main diagnostic focus for A3 is confirming that any near-well upward propagation remains limited and does not evolve into a connected vertical migration pathway, which is best evaluated using near-well vertical cross-sections and saturation or CO_2 mole-fraction indicators.

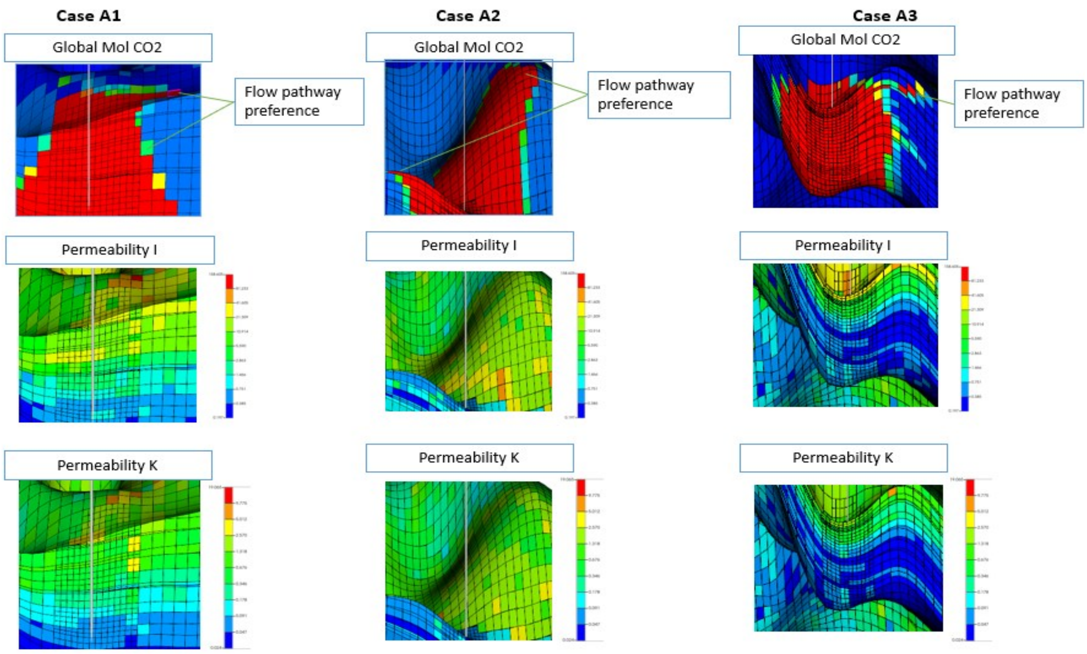

Figure 5. Preferential flow pathways and permeability controls for well placement scenarios. (a) Case A1, (b) Case A2, and (c) Case A3. For each case, the upper panel shows the CO_2 preferential flow pathway, while the middle and lower panels show the corresponding horizontal (k_i) and vertical (k_v) permeability distributions, respectively. The color scales represent permeability magnitude (mD), highlighting heterogeneity and anisotropy that govern CO_2 migration behavior.

Trapping contributions

Case A1 stores the most CO_2 and also has the largest solubility and hysteresis contributions (Figure 6). That combination is consistent with an injector location that provides better pressure dissipation (larger connected support volume/ higher effective transmissibility), allowing it to sustain higher rates for longer before being restricted by the BHP cap. In addition, A1's higher solubility and residual trapping imply greater CO_2–brine contact and broader saturation redistribution over time, which is typical when the plume spreads through multiple connected pathways rather than being confined to a single dominant high-mobility feature. In short, A1 likely had the best injectivity under the BHP constraint, producing the highest cumulative injected CO_2 and therefore the highest total stored.

Case A2 stores the least CO_2 across nearly all trapping categories, which is what we expect for a well placed near the reservoir edge. Near an edge, the system often behaves more like a semi-closed system in practice. There is less connected pressure -support volume on the "outside" side, and pressure diffusion has fewer available directions. As a result, near-well pressure rises more rapidly, the well hits the BHP limit earlier and more frequently, and the simulator reduces the injection rate more aggressively. That reduces cumulative injected CO_2 and, in turn, total stored. The lower dissolution and residual components are also consistent with a case where injection becomes pressure-limited early, restricting the plume's ability to contact large brine volumes and limiting the spatial extent of capillary immobilization.

Case A3 sits between A1 and A2 in total stored, but it has the highest supercritical-phase amount and lower solubility than A1. This pattern is consistent with a location where cumulative injection is reasonably good (so the supercritical stored is large). However, the plume remains more localized and achieves less brine-contact area than A1, reducing dissolution and residual trapping relative to A1. In a BHP-limited setting, that can happen when the injector has decent injectivity (so it can inject a lot), yet the flow architecture and anisotropy concentrate CO_2 within a smaller connected volume, preserving more CO_2 as a mobile/supercritical phase rather than distributing it broadly into brine-contacting regions.

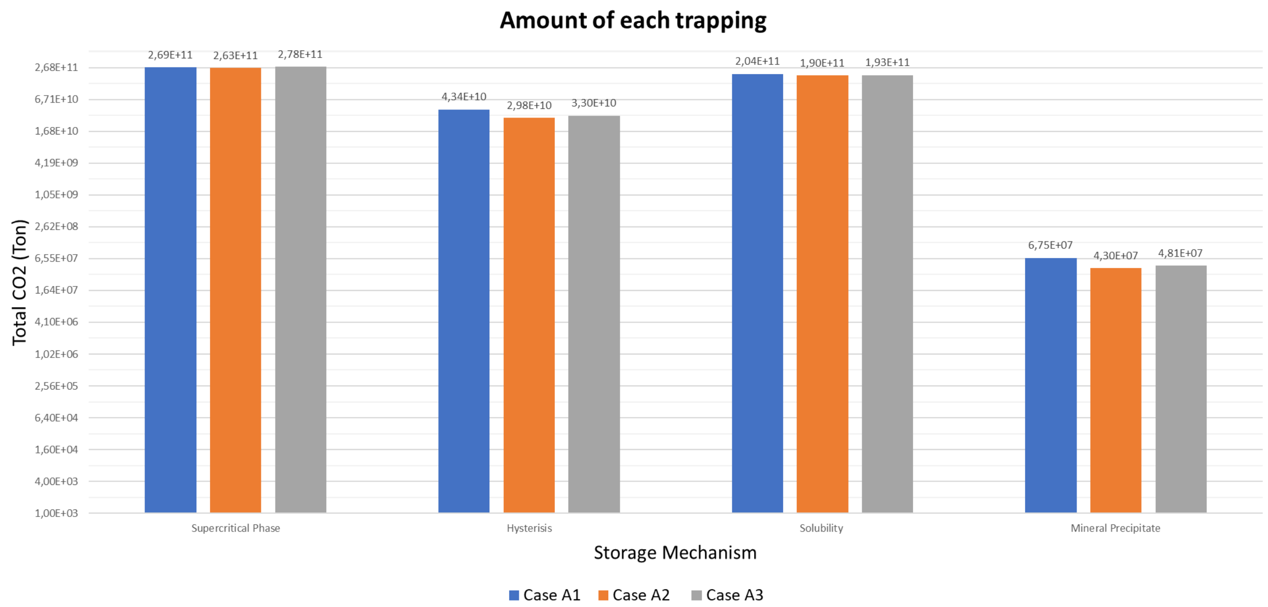

Figure 6. Contribution of CO_2 trapping mechanisms for well placement scenarios. Bar chart showing the distribution of CO_2 stored in different trapping mechanisms—structural (supercritical/free-phase), residual (hysteresis), solubility, and mineral trapping—for Cases A1, A2, and A3 at the end of the simulation period. Values represent the total mass of CO_2 stored (ton) in each mechanism.

Figure 6. Contribution of CO_2 trapping mechanisms for well placement scenarios. Bar chart showing the distribution of CO_2 stored in different trapping mechanisms—structural (supercritical/free-phase), residual (hysteresis), solubility, and mineral trapping—for Cases A1, A2, and A3 at the end of the simulation period. Values represent the total mass of CO_2 stored (ton) in each mechanism.

Single Injector with Production Scenario

This scenario is compared directly with the base case to assess how gas production near the injector modifies reservoir pressure and alters CO_2 plume movement. The objective is to quantify the benefits of pressure relief, plume steering toward the producer, and any incremental improvement in storage performance relative to the base case.

Plume steering effectiveness

Compared with baseline Case A1, Case B1 exhibited limited plume steering effectiveness (Figure 7), indicating that the addition of a single gas producer in the hydrocarbon zone did not substantially alter the overall CO_2 migration pattern by the end of the simulation period on 1 January 2145. The principal geometric difference was a slight advancement of the plume front by approximately one grid block, with no clear evidence of major plume deflection, pronounced asymmetry, or preferential migration toward the producer. This result suggests that the pressure sink induced by production was insufficient to override the primary controls on plume evolution, which remained dominated by buoyancy, reservoir structure, local topography, and permeability architecture. Although the injector–producer spacing of 1,545.39 m allowed some degree of hydraulic communication, it did not generate a sufficiently strong lateral gradient to impose meaningful directional control on plume development. Overall, the plume response indicates that geological controls remained dominant in Case B1, while the producer-induced steering effect was present but weak.

Compared with baseline Case A2, Case B2 exhibited only limited lateral plume steering despite a much stronger production-induced pressure perturbation (Figure 8). The mapped CO_2 distribution indicates that the plume front advanced by only approximately one grid block relative to A2, suggesting that the addition of a gas producer did not substantially redirect plume migration in the horizontal sense. However, the plume in B2

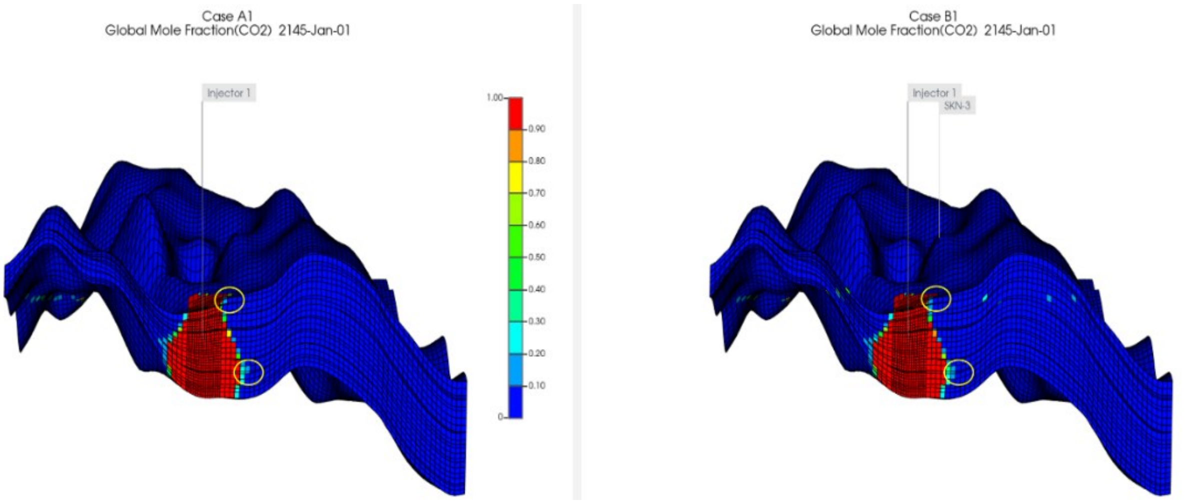

Figure 7. Comparison of CO_2 plume distribution between Case B1 and Case A1 at the end of the simulation period (2145). Spatial distribution of CO_2 global mole fraction showing plume extent for (left) Case A1 (injection only) and (right) Case B1 (injection with gas production). Highlighted regions indicate differences in plume migration and redistribution between the two cases.

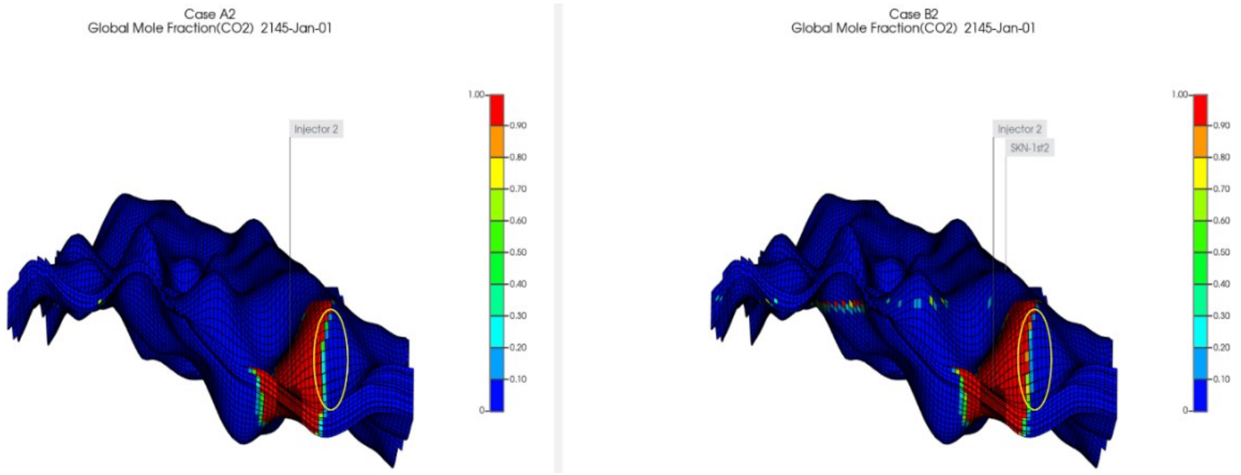

Figure 8. Comparison of CO_2 plume distribution between Case B2 and Case A2 at the end of the simulation period (2145). Spatial distribution of CO_2 global mole fraction for (left) Case A2 (injection only) and (right) Case B2 (injection with gas production). Highlighted regions indicate differences in plume migration, particularly in plume elongation and directional spreading.

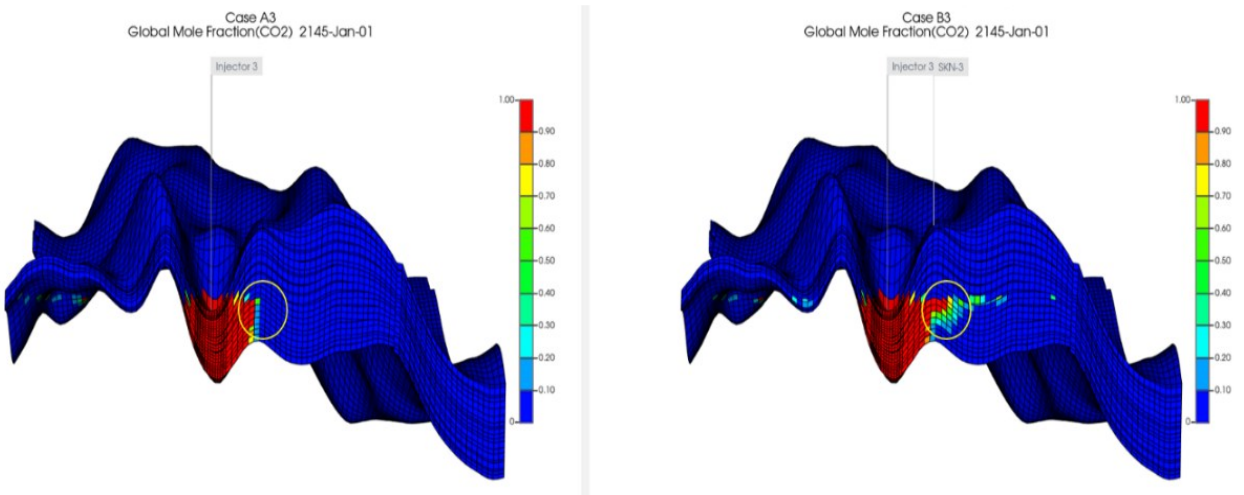

Figure 9. Comparison of CO_2 plume distribution between Case B3 and Case A3 at the end of the simulation period (2145). Spatial distribution of CO_2 global mole fraction for (left) Case A3 (injection only) and (right) Case B3 (injection with gas production). Highlighted regions indicate significant differences in plume redistribution, particularly in lateral expansion and directional migration.

became more extensive vertically, indicating that the system response was expressed more clearly through vertical redistribution than through lateral displacement. This behavior suggests that the pressure sink generated by the producer was insufficient to overcome the dominant geological controls governing plume migration, including buoyancy, structural configuration, local topography, and permeability architecture. Instead, the depletion effect appears to have modified the local pressure–mobility balance, allowing greater vertical accommodation of the plume within the available stratigraphic and structural framework. Thus, Case B2 can be interpreted as showing weak to moderate plume steering overall, with the main response occurring through vertical plume development rather than strong horizontal attraction toward the producer.

Compared with baseline Case A3, Case B3 exhibited the strongest plume-steering response among all producer-assisted scenarios (Figure 9). Although the producer-induced pressure perturbation was modest, the CO_2 plume advanced by several grid blocks and became more extensive in both the lateral and vertical directions by the end of the simulation period on 1 January 2145. This response is substantially more pronounced than that observed in B1, where the plume advanced by only about one grid block, and in B2, where the principal change was expressed mainly as greater vertical extent with only limited lateral displacement. The B3 result indicates that the producer was able to impose a strong local directional influence on the migrating plume, even though it did not substantially depressurize the reservoir at a broader scale. This suggests that plume migration in B3 was highly sensitive to local pressure gradients established near the natural migration corridor, likely amplified by the short injector–producer spacing of 887.44 m and the local structural setting. Accordingly, Case B3 can be interpreted as a scenario in which production primarily affected plume geometry rather than reservoir-wide pressure behavior, resulting in the most effective plume steering but not the strongest pressure-management performance.

Pressure reduction efficiency

This limited plume response is consistent with the moderate pressure reduction observed in Case B1 relative to Case A1 (Figure 10). The pressure difference data indicate reductions of 199.46 kPa at the reservoir top and 274.24 kPa near the injector, confirming that gas-zone production provided measurable hydraulic relief to the injection system. However, the magnitude of this relief remained modest relative to the initial reservoir pressure of 27,545.3 kPa at 2,169.95 m, with the near-injector reduction representing only about 1.0% of the initial pressure. These results indicate that the production well contributed to pressure dissipation, but not to a degree sufficient to significantly unload the injector region or fundamentally alter reservoir pressure behavior. The relatively subtle contrast observed in the pressure maps supports this interpretation. From a physical perspective, the moderate response likely reflects only partial pressure communication between the gas zone and the water leg, influenced by well spacing, reservoir architecture, and the separation between the production and injection intervals. Therefore, while Case B1 demonstrates that gas-zone production can improve pressure management, the efficiency of this mechanism in the present configuration remains limited.

The limited lateral plume response in B2 contrasts with a clearly stronger pressure-management effect relative to both A2 and the previously discussed B1 case. Reservoir pressure decreased by 1,059.73 kPa at the reservoir top and by 1,033.05 kPa near the injector, representing the largest pressure reduction observed among the B-cases (Figure 11). When normalized to the initial reservoir pressure of 27,545.3 kPa, the near-injector pressure reduction is approximately 3.75%, indicating a pressure-relief effect that is no longer minor but operationally significant for injection management. In comparison with B1, B2 delivered about 5.3 times greater pressure reduction at the top and about 3.8 times greater relief near the injector, demonstrating that the B2 well pairing provided substantially more effective hydraulic unloading of the injection system. This result suggests stronger regional pressure communication between the producer and injector, likely associated with more favorable structural connectivity, transmissibility pathways, or reservoir architecture, despite the much larger injector–producer spacing of 4,298.56 m. The B2 response, therefore, highlights that pressure-management efficiency is governed less by straight-line well distance alone than by the quality of hydraulic communication within the reservoir system.

In contrast to its strong influence on plume redistribution, Case B3 produced only limited pressure relief relative to Case A3 (Figure 12). The pressure reductions were 203.01 kPa at the reservoir top and 244.95 kPa near the injector, which are of the same order as B1 and substantially smaller than the approximately 1 MPa reductions observed in B2. Compared with the initial reservoir pressure of 27,545.3 kPa, the near-injector pressure reduction in B3 amounts to approximately 0.89%, confirming that the depletion effect remained weak from a bulk pressure-management perspective.

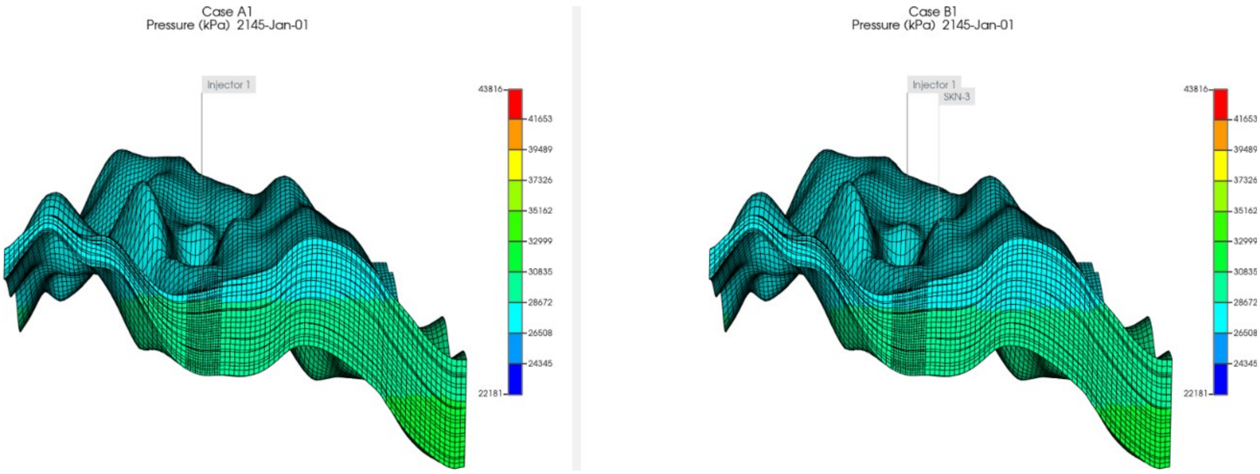

Figure 10. Comparison of reservoir pressure distribution between Case B1 and Case A1 at the end of the simulation period (2145). Spatial distribution of pressure (kPa) for (left) Case A1 (injection only) and (right) Case B1 (injection with gas production), illustrating the effect of pressure relief on reservoir pressure buildup.

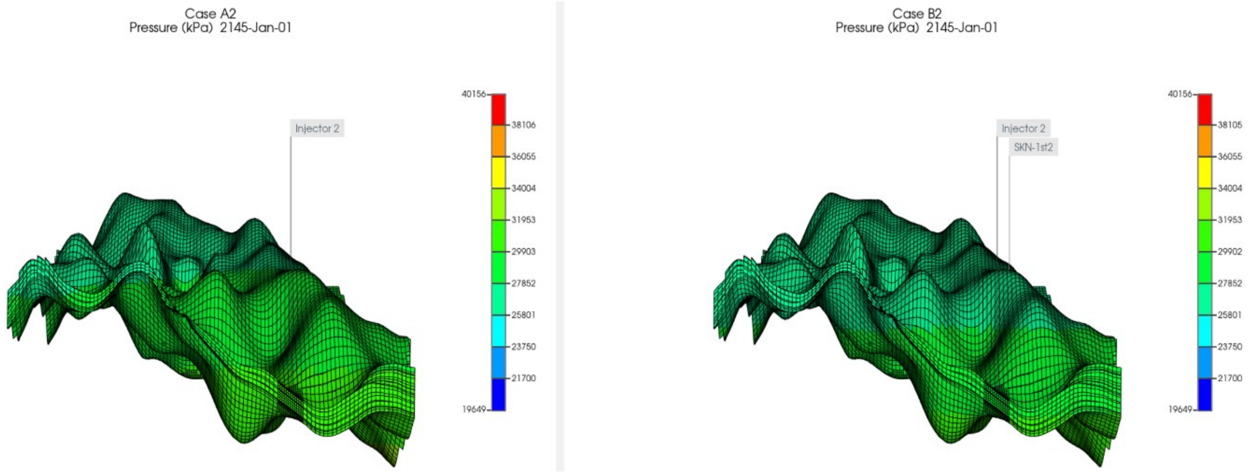

Figure 11. Comparison of reservoir pressure distribution between Case B2 and Case A2 at the end of the simulation period (2145). Spatial distribution of pressure (kPa) for (left) Case A2 (injection only) and (right) Case B2 (injection with gas production), highlighting the effect of production-induced pressure gradients on reservoir pressure redistribution.

This result is particularly notable because B3 had the shortest injector–producer spacing among the B -cases, yet did not deliver the strongest hydraulic unloading. The outcome indicates that shorter distance alone does not guarantee efficient pressure dissipation; rather, the effectiveness of pressure management depends on the degree of regional hydraulic communication and the producer's structural position within the connected pressure system. In B3, the producer appears to have generated a localized sink capable of influencing the plume trajectory, but not one sufficiently well-connected to provide substantial reservoir-scale pressure reduction. Therefore, Case B3 should be classified as having weak-to-moderate pressure-reduction efficiency, despite its strong plume response.

Incremental storage capacity

The modest pressure relief achieved in Case B1 translated into a correspondingly small increase in storage performance. Total CO_2 stored increased from 5.16×10^{11} ton in Case A1 to 5.17×10^{11} ton in Case B1, corresponding to an incremental gain of 1.0×10^{9} ton, or approximately 0.19% (Figure 13).

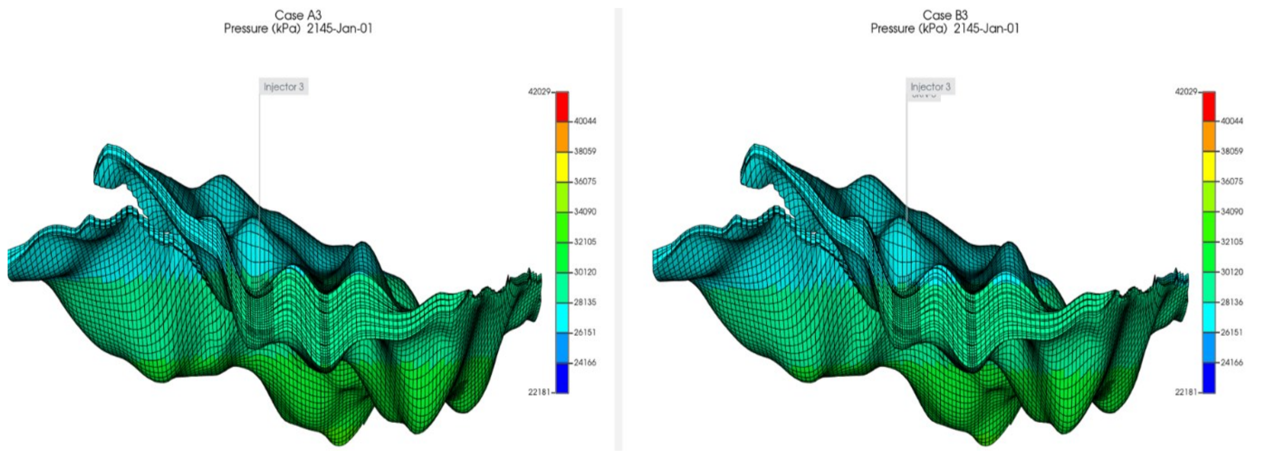

Figure 12. Comparison of reservoir pressure distribution between Case B3 and Case A3 at the end of the simulation period (2145). Spatial distribution of pressure (kPa) for (left) Case A3 (injection only) and (right) Case B3 (injection with gas production), highlighting the impact of stronger pressure gradients on reservoir pressure redistribution.

This positive but marginal increase indicates that the pressure reduction created slightly more storage capacity, but not enough to produce a substantial enhancement in injectivity or overall reservoir utilization. The trapping distribution further clarifies the nature of this gain. Relative to A1, Case B1 showed slight increases in supercritical and hysteresis trapping, accompanied by small reductions in solubility and mineral trapping. This pattern suggests that the additional stored CO_2 was retained primarily as free-phase and residually trapped CO_2, rather than being preferentially converted into dissolved or mineralized forms. Consequently, the incremental storage benefit in B1 reflects a minor extension of storage capacity under improved pressure conditions rather than a significant shift toward more secure long-term trapping mechanisms. Taken together, these results indicate that Case B1 provides a measurable but limited improvement over the baseline, with its principal benefit arising from modest pressure management rather than strong plume control or a substantial increase in storage capacity.

The substantial pressure relief in Case B2 translated directly into a meaningful increase in storage performance. Total CO_2 stored increased from 4.83×10^{11} ton in Case A2 to 5.02×10^{11} ton in Case B2, corresponding to an incremental gain of 1.9×10^{10} ton, or approximately 3.93%. This increase is markedly larger than that observed for B1 relative to A1, confirming that B2 provided a substantially more effective pressure-management benefit in terms of usable storage capacity. The trapping distribution further indicates that this gain was not simply associated with greater free-phase accumulation. Relative to A2, Case B2 showed a slight decrease in supercritical trapping, but a strong increase in hysteresis trapping and a moderate increase in solubility trapping, while mineral trapping decreased slightly. This pattern indicates that the additional stored CO_2 in B2 was redistributed toward more immobilized and dissolved forms rather than remaining predominantly in the mobile supercritical phase. From a storage-security perspective, this is a favorable outcome, as it implies that improved pressure management enhanced both storage capacity and the proportion of CO_2 retained by more stable trapping mechanisms. Taken together, these results indicate that Case B2 represents a strong pressure-management scenario in which production-induced depletion substantially improved storage efficiency. At the same time, plume response remained moderate, primarily expressed through vertical rather than lateral redistribution.

The modest pressure-relief benefit in Case B3 was accompanied by essentially unchanged total storage performance, albeit slightly lower than in Case A3. Total CO_2 stored decreased from 5.04 × 10^{11} ton in A3 to 5.03 × 10^{11} ton in B3, corresponding to a difference of -1.0 × 10^9 ton, or approximately -0.20%. Although this reduction is very small and indicates that the two cases are nearly equivalent in total storage performance, the direction of change confirms that B3 did not improve storage capacity. The trapping distribution is consistent with the plume's stronger geometric redistribution. Relative to A3, Case B3 showed slight increases in supercritical and hysteresis trapping, together with slight decreases in solubility and mineral trapping. This pattern suggests that the production-assisted configuration promoted broader migration and some additional residual immobilization along the plume path, but did not enhance dissolution-based storage. Instead, the redistributed CO_2 remained more strongly associated with the free-phase supercritical component, indicating that B3 primarily altered plume geometry rather than improving long-term trapping quality or increasing storage efficiency. Taken together, these results indicate that Case B3 is valuable mainly as a plume-control scenario. Its primary benefit lies in its ability to influence migration direction and plume extent, whereas its contribution to pressure management and incremental storage capacity remains limited.

Completion design

This scenario evaluates how changing the injector completion length, represented by the number of perforations, affects CO_2 injectivity, cumulative stored mass, and plume behavior under the same operating constraints. It provides a direct comparison with the base well-placement cases by isolating completion effects on the pressure footprint, the areal plume extent, the containment margin to the free-water level, and the evolution of trapping contributions.

Plume geometry

Case C1 (Figure 14) exhibits a clear containment trade-off relative to A1, where the plume expands both upward and outward, with vertical spread increasing from 196.22 m to

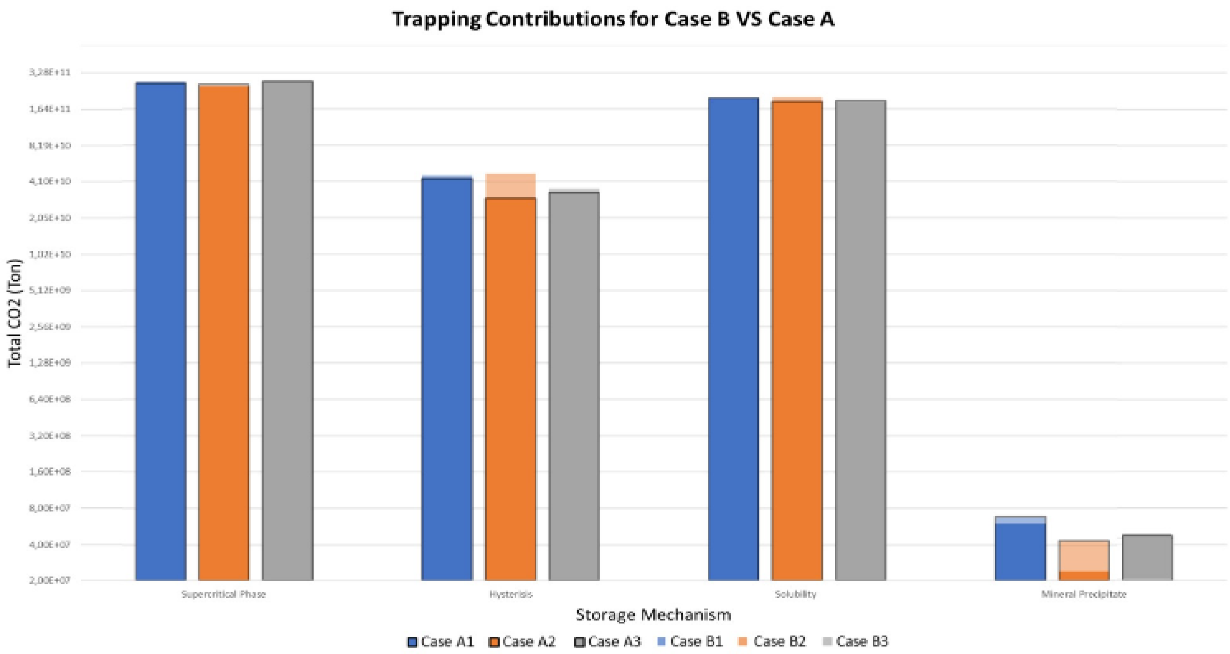

Figure 13. Comparison of CO_2 trapping contributions between production-assisted cases (B1–B3) and injection-only cases (A1–A3). Bar chart showing the distribution of CO_2 stored in structural (supercritical/free-phase), residual (hysteresis), solubility, and mineral trapping mechanisms for each case at the end of the simulation period. Values represent total stored CO_2 mass (ton).

220.126 m (Δ 23.9 m, ~12%) and lateral extent increasing from 1,605.47 m to 2,142.12 m (Δ 536.65 m, ~33%). This behavior is consistent with higher injected CO_2 mass and stronger near-well pressure gradients. At the same time, longer completions with more perforations distribute inflow across more layers and grid cells, increasing the likelihood of connecting to high-permeability streaks that then dominate preferential plume growth. In the containment view, C1 also shows localized CO_2 presence near or slightly above the free-water level (FWL) at two small spots, implying limited gas-zone encroachment that is more consistent with heterogeneity-controlled vertical conduits (e.g., locally elevated (kv), partially effective baffles, or narrow structural connectivity) rather than uniform upward migration; A1 remains more confined because its plume height and footprint are smaller.

A key evaluation is that the vertical spread is unchanged between A2 and C2 (both 323.96 m), even though injectivity is higher in C2. This indicates that vertical migration is controlled by the same geological constraints in both cases (e.g., the same vertical permeability structure, internal barriers, and buoyancy pathway limits tied to structural geometry and proximity to the free-water level), so the longer completion increases throughput. Still, it does not create a new vertical pathway (Figure 15). The additional injected CO_2 therefore primarily manifests as lateral growth, with plume width increasing from 1,809 m (A2) to 2,148.50 m (C2), an increase of 339.50 m, or about 18.8%. From a containment perspective, C2 remains within the aquifer and shows no clear breakthrough into the gas zone in the maps, but the margin to the gas zone or free-water level remains inherently tight at this location. Even without added plume height, the wider footprint can increase containment concerns by increasing the likelihood of intersecting localized high-vertical-permeability features that could act as vertical conduits, while also expanding the area of review and the monitoring burden.

C3 shows broader plume growth than A3 in both vertical and lateral directions, consistent with the higher injected mass (Figure 16). The vertical spread increases from 141.25 m (A3) to 170.579 m (C3), a rise of 29.329 m (about 20.8%), while plume width increases from 1,029 m to 1,292 m, an increase of 263 m (about 25.6%). Despite this growth, the plume crest in C3 remains clearly below the free-water level, maintaining a comfortable separation from the gas zone, which is a favorable outcome because the capacity gain is achieved without compromising the tight vertical

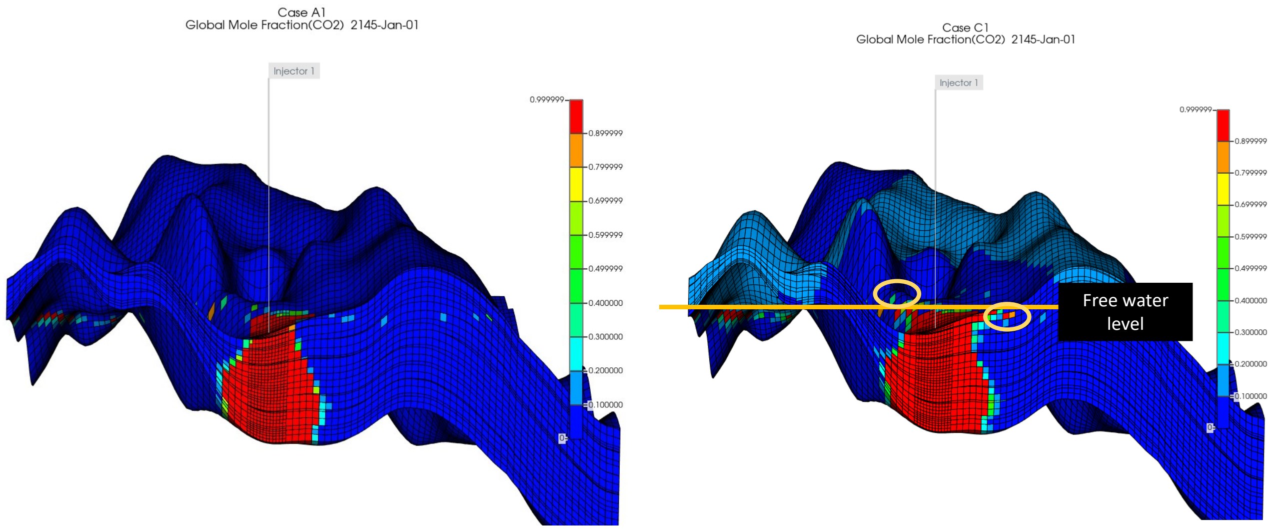

Figure 14. Comparison of CO_2 plume geometry between Case C1 and Case A1 relative to the free water level (FWL) at the end of the simulation period (2145). Spatial distribution of CO_2 global mole fraction for (left) Case A1 (baseline injection) and (right) Case C1 (modified completion). The horizontal line indicates the FWL. Highlighted regions show differences in plume vertical extent and proximity to the FWL, illustrating the impact of completion design on upward plume migration and containment.

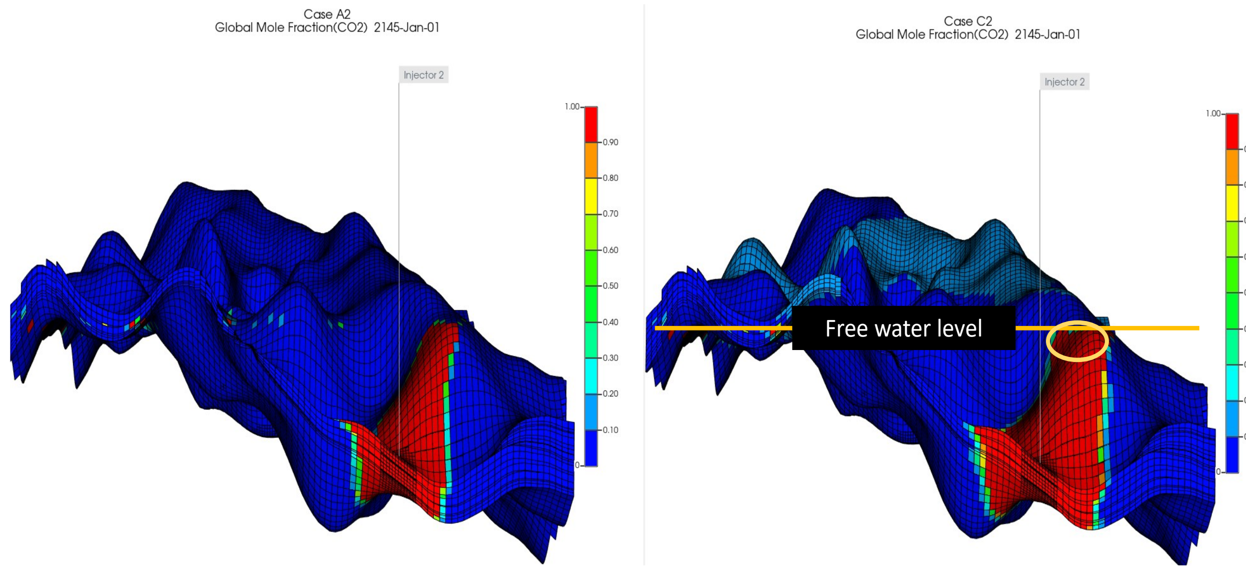

Figure 15. Comparison of CO_2 plume geometry between Case C2 and Case A2 relative to the free water level (FWL) at the end of the simulation period (2145). Spatial distribution of CO_2 global mole fraction for (left) Case A2 (baseline injection) and (right) Case C2 (modified completion). The horizontal line represents the FWL. Highlighted regions indicate differences in plume height and lateral extent, demonstrating how changes in completion affect plume distribution and vertical confinement below the gas zone.

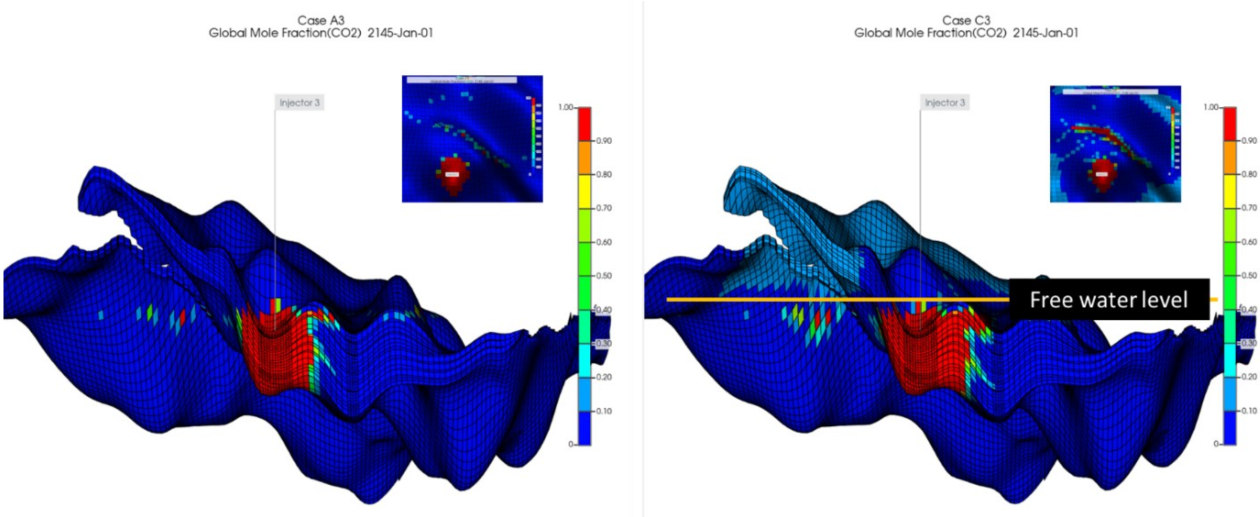

Figure 16. Comparison of CO_2 plume geometry between Case C3 and Case A3 relative to the free water level (FWL) at the end of the simulation period (2145). Spatial distribution of CO_2 global mole fraction for (left) Case A3 (baseline injection) and (right) Case C3 (modified completion). The horizontal line denotes the FWL. Highlighted regions emphasize variations in plume geometry, particularly vertical rise and lateral spreading, indicating the effect of completion design on plume containment and migration behavior.

containment margin. In plan view, C3 also develops a distinct, concentrated CO_2 patch to the north that is weak in A3, which is most consistently interpreted as activation of a preferential lateral corridor at higher injectivity, such as a locally higher-permeability trend or a better-connected transmissibility pathway. With less injected mass in A3, the pressure gradients are insufficient to drive this pathway strongly. In contrast, in C3, the higher pressure-gradient field and increased CO_2 supply enable the plume to access it and develop into a secondary lobe. This feature is better interpreted as a lateral diversion rather than a vertical escape, since vertical containment remains secure; however, it does imply a larger areal footprint and area of review, so the monitoring design should explicitly account for the possibility of a secondary lobe when injection is intensified.

Injectivity

Increasing the perforation count improved injectivity and therefore increased the total CO_2 stored under the same operating constraints: C1 stored (6.61×10^{11}) ton, while A1 stored (5.16×10^{11}) ton by 1 January 2145, corresponding to an incremental storage of (1.45×10^{11}) ton (about 28% higher than A1). Mechanistically, tripling perforations reduces near-wellbore flow resistance (lower entry losses and lower effective skin), allowing more CO_2 to enter the formation before reaching the bottom-hole pressure (BHP) limit, thereby expanding the pressure and plume footprints and increasing sensitivity to reservoir heterogeneity. Within the completion-sensitivity set (Table 2), C1 still exhibits the lowest injectivity, with II = 5.86 m^3/day/kPa early and 8.45 m^3/day/kPa late; the low early-time II (Figure 17) indicates a near-well-dominated regime where higher BHP buildup is needed to sustain injection, consistent with local heterogeneity, weaker connection to the best-flowing layers, or higher effective entry loss. Over time, II increases by 2.59 m^3/day/kPa (about 44%), indicating a shift toward a more reservoir-controlled regime as a larger connected volume supports flow. However, C1 remains slightly behind the other completion cases in overall injectivity.

For the C2 versus A2 comparison, the longer completion again acts as a first-order driver of performance: C2 stores 6.19×10^{11} ton versus 4.83×10^{11} ton in A2, giving an incremental storage of 1.36×10^{11} ton (about 28% higher), which is most consistently explained by reduced near-wellbore flow resistance in C2 because the larger perforated interval increases reservoir contact area, lowers entry losses, and allows more CO_2 to enter the formation under the same constraints and timeframe. In injectivity terms, C2 is moderately stronger than C1, with II = 6.14 m^3/day/kPa early and 8.56 m^3/day/kPa late, indicating slightly easier near-well entry (less pressure buildup needed early) but a very similar late-time behavior once injection becomes reservoir-controlled, implying that C1 and C2 are ultimately supported by comparable reservoir-scale transmissibility and connectivity despite the early-time advantage in C2.

For the C3 versus A3 pair, the longer completion produces the largest storage uplift among the completion-sensitivity comparisons, consistent with A3 being more completion-limited (higher entry losses and weaker near-well connection), such that adding perforations significantly improves well–reservoir contact and reduces near-well pressure drop. As a result, C3 stores (6.72×10^{11} ton compared with 5.04×10^{11} ton in A3, an incremental gain of 1.68×10^{11} ton (about 33.3%), under the same project duration and operating constraints. This is reinforced by injectivity behavior: C3 is the injectivity leader, with II = 8.24 m^3/day/kPa early and 9.86 m^3/day/kPa late, implying substantially lower pressure buildup is required to sustain injection, consistent with a more favorable near-well environment (better connection to high-permeability layers and lower effective flow resistance) and a reservoir region with stronger transmissibility/pressure support; the relatively smaller early-to-late II increase (1.62 m^3/day/kPa, ~20%) further indicates that C3 initiates at high efficiency and sustains it throughout production, rather than depending on a delayed reservoir-drive contribution at late times.

Table 2. Injectivity index among different cases

No	Period	Injectivity index (II, m^3/day/kPa)		
		C1	C2	C3
1	Early-time II (near-well dominated)	5,86	6,14	8.24
2	Late-time II (reservoir dominated)	8,45	8,56	9.86

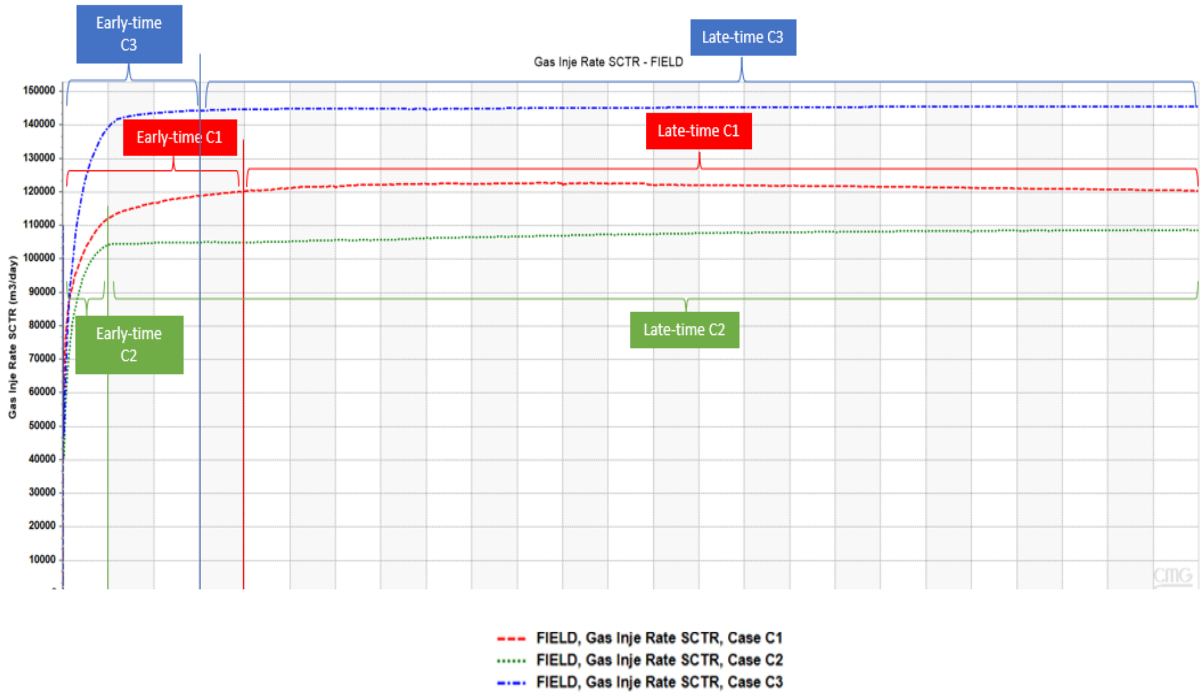

Figure 17. Comparison of CO_2 injection rate evolution for completion scenarios (Cases C1–C3). Time series of field gas injection rate (Sm³/day) showing early-time and late-time behavior for Cases C1, C2, and C3. The curves illustrate differences in injectivity and rate stabilization associated with completion design.

Trapping contributions

Relative to A1, C1 stores about 28% more CO_2 (Figure 18). The stored CO_2 is still dominated by structural or free-phase (supercritical) CO_2, which is typical when injection is more effective, and a larger connected CO_2 phase is maintained in the pore space. The most significant change is the considerable increase in residual trapping (hysteresis). Residual trapping grows much faster than total storage, which indicates a larger two-phase swept volume and stronger saturation redistribution during migration and post-injection relaxation. In practical terms, the completion change expands the region that experiences CO_2–brine displacement, so more CO_2 becomes immobilized as disconnected blobs at the trailing edge of the plume. Solubility trapping increases, but its growth is smaller than that of free-phase CO_2. This suggests that the incremental CO_2 in C1 increases plume volume more rapidly than it increases effective CO_2–brine interfacial contact for dissolution over the same time window. Mineral trapping increases slightly and remains negligible on this timescale, consistent with slow reaction rates in field-scale reactive transport settings.

Relative to A2, C2 also stores about 28% more CO_2. Structural or free-phase CO_2 remains the largest component, but C2 shows the strongest upward shift in residual trapping contribution. Residual trapping approximately doubles, and its fraction of total stored CO_2 increases from about 6% to about 10%. This pattern is consistent with a broader immiscible displacement footprint, indicating that more reservoir volume experiences simultaneous CO_2 and brine flow. That creates more opportunity for capillary trapping as saturations relax after injection and local mobility decreases. Solubility trapping increases in absolute terms, but its fraction decreases slightly. This implies that incremental CO_2 increases plume extent and CO_2 saturation more rapidly than it increases long-term dissolution capacity over the evaluated period. Mineral trapping increases but remains a very small fraction of storage.

Relative to A3, C3 stores about 33% more CO_2. The incremental stored CO_2 is dominated by structural or free-phase (supercritical) CO_2, which indicates that the completion change primarily increases connected CO_2 saturation and plume volume. Residual trapping increases significantly, indicating continued expansion of the two-phase swept zone. However, its fraction increases only modestly because free-phase CO_2 increases more strongly. Solubility trapping increases, but it does not keep pace with the increase in free-phase CO_2. This suggests that plume growth and associated CO_2 saturation increase more rapidly than dissolution-driven trapping over the same time horizon. Mineral trapping increases in absolute terms and remains negligible relative to structural, residual, and solubility trapping.

Objective fulfillment, response to the problem statement, and broader relevance to CCS

This study was designed to address a central operational problem in aquifer-zone CO_2 storage in depleted gas reservoirs: how to improve storage performance while ensuring that the injected plume remains confined within the aquifer zone and does not migrate into the overlying hydrocarbon interval. A second linked problem concerned whether operational design changes could meaningfully improve long-term trapping performance, particularly mineral trapping, under realistic pressure and containment constraints. These questions are directly consistent with the study objective, namely, to identify an optimized injection strategy that is pressure-safe, containment -secure, and capable of improving long-term storage performance.

The simulation results show that the problem of aquifer-zone plume containment can be addressed through operational design, but that different design variables control different parts of performance. Among the baseline well-placement cases, A3 exhibited the most favorable containment behavior, as indicated by its smallest lateral footprint and vertical plume spread. This shows that injector placement within the aquifer is a first-order control on plume geometry and the risk of upward migration. In contrast, A1 delivered the highest total stored CO_2 among the baseline cases, indicating that the configuration that maximizes storage volume is not necessarily the same as the one that maximizes containment security. This distinction is important because it demonstrates that storage design in gas-reservoir aquifers must be evaluated as a multi-criteria problem rather than a single-capacity problem.

The results also answer whether pressure management through production can improve storage performance. The production-assisted cases show that gas production can reduce pressure buildup, but its effectiveness depends strongly on the quality of hydraulic communication rather than injector–producer distance alone. Case B2 provided the strongest pressure-management benefit, produced the largest pressure reduction, and increased total stored CO_2 relative to its baseline counterpart. However, B3 produced the clearest plume-steering response while contributing only limited pressure relief and no meaningful storage gain. These contrasting outcomes show that pressure reduction, plume steering, and storage increase are related but not identical objectives. Accordingly, production coupling should be viewed as a selective design tool whose value depends on whether the primary operational target is pressure relief or directional plume control.

With respect to completion design, the study demonstrates that completion modification produced the largest storage improvement of all scenario groups, increasing total stored CO_2 by about 28–33.3% relative to the corresponding baseline cases. The main mechanism was improved injectivity through reduced near-well flow resistance and increased reservoir contact. At the same time, the completion results show that higher injectivity can enlarge plume extent and, in some cases, reduce the local containment margin. This is illustrated most clearly by C1, which showed localized upward CO_2 occurrence near the free-water level. Therefore, completion redesign can be highly beneficial for increasing storage throughput, but it must be applied together with careful containment screening and monitoring design.

The study further addresses whether the tested strategies substantially enhanced mineral trapping. The results indicate that mineral trapping increased only slightly within the 120-year simulation period, even in the better-performing cases. This means that mineral trapping, while favorable, did not become the dominant mechanism controlling storage performance over the evaluated timescale. Instead, the main performance gains were achieved through better plume control, improved injectivity, pressure management, and increased contributions

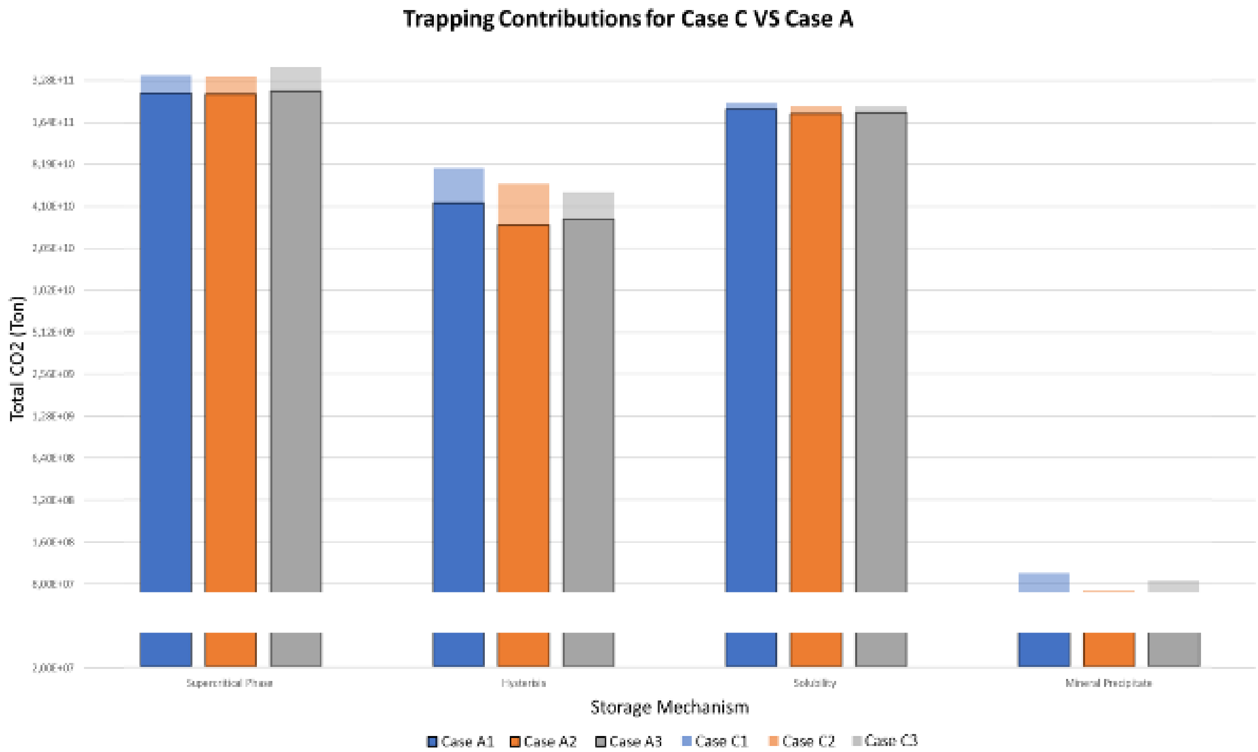

Figure 18. Comparison of CO_2 trapping contributions between completion scenarios (Cases C1–C3) and baseline injection cases (A1–A3). Bar chart showing the distribution of CO_2 stored in structural (supercritical/free-phase), residual (hysteresis), solubility, and mineral trapping mechanisms at the end of the simulation period. Values represent the total stored CO_2 mass (ton) for each case.

from supercritical, residual, and solubility trapping. Thus, the study shows that in this type of reservoir system, operational optimization can improve conditions that support long-term secure storage. Still, mineral trapping itself remains kinetically limited within the modeled project duration.

In relation to the article's theme and title, the findings strongly support the argument that optimizing CO_2 storage strategies in Indonesian gas -reservoir aquifers requires simultaneous consideration of plume containment and trapping behavior, rather than focusing solely on storage volume. The title emphasizes both enhanced mineral trapping and plume containment, and the results clarify their relationship: plume containment can be substantially improved through well placement and selective pressure management. In contrast, mineral trapping can be improved only modestly over the simulated timeframe. This does not weaken the title; rather, it sharpens the scientific message by showing that plume containment is the dominant short- to medium-term operational lever, whereas mineral trapping is a slower, long-term benefit that may be incrementally supported but not rapidly transformed by operational design.

More broadly, the study contributes to CCS by showing that aquifer-zone storage in gas reservoirs should be assessed using an integrated decision framework that combines containment security, pressure safety, injectivity, and trapping evolution. The results demonstrate that a scenario may perform well in one dimension but not in another, so site-development decisions should be based on balanced, constraint-based optimization rather than on maximum injected mass alone. This has practical implications for CCS project screening, operational planning, and risk management, especially in mature gas fields where the storage objective must coexist with strict containment requirements. For CCS in general, the work highlights that safe and effective storage depends not only on theoretical capacity, but on the ability to operate within a pressure-safe envelope, preserve plume confinement, and select well configurations that align storage efficiency with long-term containment security. In this sense, the study contributes a practical workflow for translating storage potential into a more realistic, operationally defensible CCS design.

CONCLUSION

This study evaluated CO_2 storage optimization strategies in the aquifer zone of the SK gas reservoir under a common safe operating pressure envelope and a strict containment requirement that the plume remain within the aquifer zone throughout the 120-year simulation period. The results show that storage performance in this system is governed by a trade-off among plume containment, pressure management, and injectivity-driven storage gain, rather than by a single universally optimal design. Most scenarios maintained plume confinement within the aquifer zone, demonstrating that aquifer-zone injection can be operated in a storage-secure manner under the tested conditions. However, localized upward CO_2 occurrence near the free-water level in Case C1 indicates that higher-injectivity designs may reduce the vertical containment margin, thereby requiring closer operational surveillance.

In the well-placement scenarios, injector location was found to exert first-order control over plume geometry and containment performance. Among the baseline cases, Case A3 provided the most favorable plume containment, with the smallest vertical spread and the most compact lateral footprint, indicating the lowest likelihood of gas-zone encroachment. In contrast, Case A1 yielded the highest total stored CO_2 among the baseline scenarios. This result demonstrates that the configuration that best minimizes plume migration is not necessarily the one that maximizes total stored mass. Therefore, the well placement should be selected based on the primary project objective.

For production-assisted injection scenarios, the results indicate that adding a gas producer can improve pressure behavior. Still, the benefit depends primarily on hydraulic communication within the reservoir rather than on injector–producer distance alone. Case B2 was identified as the most effective pressure-management scenario, producing the largest pressure reduction and a meaningful increase in total stored CO_2 relative to A2. By contrast, Case B3 showed the strongest plume-steering effect but only limited pressure relief and essentially no storage gain relative to A3. These findings indicate that production support may serve different operational functions depending on reservoir connectivity and structural setting, improving either pressure-limited storage capacity or plume redistribution, but not necessarily both simultaneously.

Among all tested strategies, completion redesign produced the largest storage gains. Cases C1–C3 increased total stored CO_2 by approximately 28–33.3% relative to their corresponding baseline cases, demonstrating that improved well–reservoir contact and reduced near-well flow resistance can substantially enhance injectivity and storage performance under the same operating constraints. Nevertheless, these gains were accompanied by broader plume footprints and, in the case of C1, localized upward CO_2 occurrence near the free-water level. This indicates that completion redesign is a highly effective means of increasing storage capacity, but its application must be balanced against containment margin and monitoring requirements.

In terms of trapping behavior, the tested strategies generally increased total stored CO_2 and promoted stronger residual trapping and, in some cases, solubility trapping, particularly as plume sweep broadened. Mineral trapping showed slight increases in some cases but remained a very small fraction of total storage over the simulated time horizon. Therefore, although the results indicate potential for enhancing long-term, permanent trapping, mineral trapping did not become a dominant storage mechanism during the 120 years considered in this study. Instead, storage security over the modeled timeframe was mainly controlled by plume containment, pressure management, and the evolution of structural, residual, and dissolved trapping.

Overall, the findings demonstrate that optimized CO_2 storage in gas-reservoir aquifer zones requires a constraint-based design approach that simultaneously evaluates containment security, pressure safety, and storage efficiency. Case A3 was the most favorable baseline option for plume containment, Case B2 was the most effective pressure-management configuration, and completion redesign was the strongest strategy for maximizing stored CO_2. These results directly address the study objectives and show that secure and efficient aquifer-zone CO_2 storage cannot be achieved solely through capacity maximization. Rather, it requires integrated optimization of well placement, pressure-management strategy, and completion design to achieve storage-secure performance under operational and geological constraints.

For CCS development more broadly, this study highlights that aquifer-zone storage in depleted or producing gas reservoirs represents a viable and optimizable storage option when supported by robust simulation-based screening and clearly defined operational constraints. The results further indicate that future work should extend the simulation period and expand the geochemical representation to better resolve long-term mineral-trapping behavior. Additional value may also be obtained by evaluating combined optimization strategies that jointly consider well placement, completion design, and pressure-management configuration, rather than treating them independently. For scenarios associated with broader plume spread or reduced vertical containment margin, monitoring and risk assessment near the free-water level should be strengthened. Overall, the findings support the use of well placement, pressure support, and completion design as complementary controls for simultaneously improving containment, injectivity, and storage capacity.

ACKNOWLEDGEMENT

The authors would like to thank the Exploration Division and the CCS Laboratory of LEMIGAS for their valuable technical and institutional support during the completion of this study. The authors also acknowledge KIGAM for its support and collaboration.

DECLARATIONS

Author contribution

Utomo Pratama Iskandar was responsible for conceptualizing the study, developing the workflow, conducting reservoir simulation, analyzing and interpreting the results, and drafting the manuscript. Arik contributed to the technical evaluation and critical revision of the manuscript. Panuju provided geological supervision. Garindia Grandis contributed to the development and upscaling of static models. All authors reviewed and approved the final manuscript.

Funding statement

None

Competing interest

None

The use of AI or AI-assisted technologies

None

GLOSSARY OF TERMS AND SYMBOLS

Terms & Symbols	Definition	Unit
FWL	Free-water level – boundary between aquifer and overlying gas zone	-
BHP	Bottom-hole pressure	psia or kPa
LGR	Local grid refinement – grid refinement around wells to capture near-well processes	-
SOPE	Safe Operating Pressure Envelope – maximum allowable injection pressure constrained by fracture, fault-slip, tensile failure, and caprock entry pressures	-
II	Injectivity index – measure of injection rate per unit pressure drawdown	m³/day/kPa
TVD	True vertical depth	ft or m
ppm	Parts per million (salinity)	ppm

J/mol	Joule per mole (activation energy)	J/mol
m^2/m^3	Square meter per cubic meter (reactive surface area)	m^2/m^3
NaCl	Sodium chloride (salt)	-
Aquifer zone	Brine-saturated portion of a reservoir beneath or laterally adjacent to a gas/oil accumulation	-
Plume	Body of injected CO_2 migrating through the reservoir	-
Mineral trapping	Permanent CO_2 storage through carbonate precipitation (e.g., calcite, dolomite)	-
Solubility trapping	CO_2 trapped by dissolution into formation brine	-
Residual trapping	CO_2 immobilized as disconnected blobs by capillary forces (hysteresis)	-
Structural trapping	CO_2 retained as a supercritical free phase beneath a caprock	-
Supercritical trapping	Same as structural trapping	-
Caprock	Low-permeability sealing formation that overlies the reservoir	-
Fracture pressure	Pressure at which rock tensile failure initiates	kPa or psia
Fault-slip pressure	Pressure that may trigger reactivation of a fault	kPa or psia
Tensile failure pressure	Pressure causing tensile failure of the rock	kPa or psia
Caprock entry pressure	Minimum pressure for CO_2 to enter caprock pores	kPa or psia
Viscosity	Fluid resistance to flow	cP or Pa·s
Salinity	Concentration of dissolved salts in formation water	ppm
k_i / k_h	Horizontal permeability	mD
k_v / k_x	Vertical permeability	mD
Kv/Kh	Ratio of vertical to horizontal permeability (anisotropy)	-

REFERENCES

Akai, T., Saito, N., Hiyama, M., & Okabe, H., (2021), Numerical modelling on CO_2 storage capacity in depleted gas reservoirs. Energies, 14(13), 3978.

Al-Hajri, M., & Al-Maldas, K., (2026), Numerical reservoir simulation of CO_2 storage in saline aquifers: Assessment of trapping mechanisms, geochemistry, O_2 impurities, and brine salinity. Processes, 14(2), 316.

Bohloli, B., et al., (2013), Field-data analysis and hydromechanical modeling of CO_2 storage at In Salah, Algeria.

Chadwick, R. A., et al., (2011), Geological characteristics and performance data of the Sleipner CCS project Utsira Sand.

Chai, M., Niu, B., & Zhang, Y., (2025), Evaluating CO2 storage strategies in saline aquifer: A simulation study on pressure, rate, and duration. Indonesian Mining Journal, 28(2).

Economic Research Institute for ASEAN and East Asia (ERIA), (2024), Comprehensive CCUS research report for the ASEAN region.

Flett, M. (2008). Subsurface development of CO_2 disposal for the Gorgon Project. Energy Procedia.

Geoquake, (2024), Indonesia earthquakes and the Ring of Fire: Unraveling the threat.

Hoteit, H., Fahs, M., & Soltanian, M. R., (2019), Assessment of CO_2 injectivity during sequestration in depleted gas reservoirs. Geosciences, 9(5), 199.

Irzon, R., et al., (2024), Prospecting CCS Project in Indonesia: A Case Study in Meratus Mountains.

Iskandar, U. P., (2009), Carbon Capture and Storage (CCS) – Enhanced Oil Recovery (EOR): Global Potential in Indonesia. *Scientific Contributions Oil and Gas*, 32(3), 228–238. https://doi.org/10.29017/SCOG.32.3.855.

Iskandar, U. P., & Kurihara, M., (2022), Long Short-term Memory (LSTM) Networks for Forecasting Reservoir Performances in Carbon Capture, Utilization, and Storage (CCUS) Operations. *Scientific Contributions Oil and Gas*, 45(1), 35–50. https://doi.org/10.29017/SCOG.45.1.943.

Iskandar, U. P., & Kurihara, M., (2025), Co-optimization of Carbon Capture, Utilization, and Storage (CCUS) Project Using Iterative

Latin Hypercube Sampling (ILHS). *Scientific Contributions Oil and Gas*, 48(2). https://doi.org/10.29017/scog.v48i2.1818.

Jang, Y., & Wang, J., (2022), Geomechanical risks potentially caused by pore pressure buildup due to CO_2 injection. Chemical Engineering Journal.

Jaya, A., (2009), Geological consideration for CO_2 storage in Indonesia: A basinal scale outlook.

Jaya, A., (2015), Geological conditions, intensity, and distribution of faults for CO_2 storage in Indonesia.

Jisc, (2024), Implications for fault locking south of Jakarta: Investigation of seismic activity along the Baribis fault.

Kazlou, T., Cherp, A., & Jewell, J., (2024), Feasible deployment of carbon capture and storage and the requirements of climate targets. Nature Climate Change, 14(10), 1047–1055.

Khanifar, A., Motaei, E., Mustapha, S., Ranjan, R., & Azman, M. F., (2024, October), Unveiling Challenges and Enhancing Robustness of CO_2 Storage Capacity Estimation in a Depleted Gas Reservoir for Storage Development Planning. In SPE Asia Pacific Oil and Gas Conference and Exhibition (p. D031S025R002). SPE.

LeksLawyer, (2023), Carbon Capture and Storage (CCS) and Carbon Capture Utilization and Storage (CCUS) potential and regulation in Indonesia.

Li, Z., Hatzignatiou, D. G., & Ehlig-Economides, C. A., (2025), Carbon-Neutral Economic Viability of Enhanced CO_2 Storage and Gas Recovery in Natural Gas Reservoirs Under Strong Bottom Water Drive. SPE Journal, 1–16.

Martin-Roberts, E., et al., (2021), Carbon capture and storage: Constraints on capacity from a geomechanical perspective. Frontiers in Energy Research.

Massagony, A., Pandit, R., & White, B., (2025), Political economy of energy policy in Indonesia towards net zero emissions by 2060. Energy for Sustainable Development, 88, 101757.

Mathieson, A., Midgley, J., Wright, I., Saoula, N., & Ringrose, P., (2011), In Salah CO_2 storage JIP: CO_2 sequestration monitoring and verification technologies applied at Krechba, Algeria. Energy Procedia, 4, 3596–3603.

Matkivskyi, S., & Burachok, O., (2022), Impact of reservoir heterogeneity on the control of water encroachment into gas-condensate reservoirs during CO_2 injection. Management Systems in Production Engineering, 1 (30), 62–68.

MDPI, (2024), Carbon transportation technologies and logistics of marine transportation for offshore CCUS.

Medeiros, S. H. S., et al., (2025), Impact of CO_2 concentration on trapping mechanisms in saline aquifers for CCS–Brazilian Journal of Petroleum and Gas, 19(3), 899.

Orrick, (2025), Navigating Carbon Capture in Indonesia: A Key Step Forward regarding regulatory frameworks.

Pasarai, U., (2014), Ranking of Indonesia Sedimentary Basin and Storage Capacity Estimates for CO_2 Geological Storage.

Pertamina, (2023), Examination of the potential and challenges of implementing CCS within a low-carbon development framework.

Ringrose, P., Atbi, M., Mason, D., Espinassous, M., Myhrer, Ø., Iding, M., & Mathieson, A., (2013), The In Salah CO_2 storage project: Lessons learned and knowledge transfer. Energy Procedia, 37, 6226–6236.

Rucci, A., Vasco, D. W., & Novali, F., (2013), Monitoring the geologic storage of carbon dioxide using surface deformation: A geomechanical analysis of In Salah, Algeria. International Journal of Greenhouse Gas Control, 12, 120–131.

Society of Petroleum Engineers (SPE), (2025), Independent study addresses causes of challenges in Asia-Pacific flagship CCS projects.

Syahbana, D. K., et al., (2019), Fracture network reactivation due to stress changes and magma intrusion in Indonesian volcanic settings.

Tatschner, K., (2025), The Sleipner CCS Project – An Active Case History for CO_2 Storage in a Saline Aquifer. C&C Reservoirs.

Turan, A., et al., (2021), Mapping the potential CO_2 source-sinks for Carbon Capture Storage from industry in Indonesia.

U.S. Department of Energy (US DOE), (2021), Meeting the Dual Challenge: Prospective geologic formations for CO_2 storage. Energy.gov.

U.S. Geological Survey (USGS), (2024), Aquifers and Groundwater: Understanding hydrogeological characteristics and zone saturation.

Van den Hoek, P. J., Sengel, A., Vlad, D., & Marian, V., (2025, June), Reservoir Cooling and Fault Stability Analysis for CO_2 Injection into Depleted Gas Reservoirs Including Joule-Thomson Effect. SPE Europe featured at the EAGE Conference and Exhibition.

Vasco, D. W., Ferretti, A., & Novali, F., (2010), Estimating permeability from quasi-static deformation: Temporal variations and arrival-time inversion. Geophysics, 75(4), O1–O13. (Applied to In Salah deformation and reservoir properties).

Wang, Y., et al., (2025), Long-distance migration assisted structural trapping during CO_2 storage in an offshore basin. Scientific Reports, 15, 28680.

White, J. A., et al., (2014), In the Salah CCS project, the geomechanical response and surface heave findings.

Worden, R. H., (2024), Carbon Dioxide Capture and Storage (CCS) in Saline Aquifers versus Depleted Gas Fields. Geosciences.

World Risk Report, (2024), Indonesia's exposure to significant seismic and volcanic activity.

Zaidin, M. F., Chapoy, A., Coquelet, C., Valtz, A., A Raub, M. R., & Kantaatmadja, B. P., (2018, October), Impact of H_2S in predicting the storage efficiency of CO_2 injection in a high pressure high temperature (HPHT) carbonate aquifer-a case study in a Sarawak offshore high CO_2 gas field, Malaysia. In the 14th Greenhouse Gas Control Technologies Conference, Melbourne (pp. 21–26).

Zhang, L., et al., (2024), Impact of rock mineralogy on reactive transport of CO_2 during carbon sequestration in a saline aquifer–Journal of Petroleum Exploration and Production Technology, 14, 1927.

Zoback, M. D., & Gorelick, S. M., (2012), Geologic carbon storage and induced seismicity risks.